Monte Carlo simulations of nanosecond electromagnetic pulse interaction with field-aligned ionospheric plasma density irregularities

M. Kirillin, E. Sergeeva, D. Kurakina, I. Zudin, and M. Gushchin

A.V. Gaponov-Grekhov Institute of Applied Physics of Russian Academy of Sciences,

46 Ulyanov Street, Nizhny Novgorod 603950, Russia

Corresponding author: Mikhail Kirillin (kirillin@ipfran.ru)

Key Points:

- Monte Carlo model of nanosecond electromagnetic pulse propagation in ionospheric plasma with field-aligned density depletions is developed

- Frequency dispersion competes with pronounced pathlength dispersion for scattered waves at low frequencies.

- The effects of density depletions on electromagnetic pulse properties seem weak even for strong plasma density depletions of up to 50%.

-

17 **Abstract**

18 We propose an approach to simulate ultra-wideband (UWB) electromagnetic pulse (EMP)
19 propagation in ionosphere with magnetic field-aligned irregularities of plasma density based on
20 Monte Carlo technique. This approach considers propagation of a nanosecond EMP by ray
21 trajectories in frequency domain, which allows one to analyze the role of scattering effects for
22 lower and higher harmonics of the pulse. Parameters of the irregularities used in the
23 simulations are chosen close to those of artificial ionospheric turbulence (AIT) density striations
24 stimulated by high-frequency (HF) heating facilities. The employed technique provides a
25 possibility to compare the effects of dispersion and scattering on a waveform of bipolar
26 nanosecond EMP for various parameters of ionospheric plasma and its disturbances. In the
27 presence of 10-meter scale, 10-percent level density striations, we show that lower frequencies
28 are most responsible for the EMP waveform transformation due to the plasma dispersion, and
29 are scattered away from the initial propagation direction, while higher frequencies experience
30 minor dispersion and are less scattered. The influence of AIT-type striations on the
31 straightforward EMP delay and its broadening in time domain is analyzed compared to the EMP
32 propagation in uniform plasma. Preliminary, the effects of AIT-type striations on EMP
33 characteristics seem to be weak in the main part of its frequency spectrum, even for strong
34 (non-realistic) plasma density depletions of up to 50%.

35

1 Introduction

37   Ultrawideband (UWB) electromagnetic pulses (EMPs) are signals with duration from
38 tens of picoseconds to several nanoseconds. The frequency spectrum of such signals is very
39 broad, from about 100 MHz to 10 GHz, since EMPs are as short as one cycle of oscillation of the
40 electromagnetic field. The development of UWB technology in recent decades (Agee et al.,
41 1998; Baum, 1992; Nekoogar, 2011) has led to discussion of the possibilities of UWB EMP use
42 for sounding the ionosphere and building trans-ionospheric radio communication channels
43 (see, for example,(Soldatov & Terekhin, 2016)). Recently, first experiment of trans-ionospheric
44 propagation of a nanosecond EMP with its reception onboard a satellite was reported (Zhang et
45 al., 2024).

46   In this regard, questions inevitably arise about the effect of ionospheric plasma on the
47 waveform and frequency spectrum of UWB EMP, primarily the effects of dispersion and
48 scattering on natural and artificial electron density irregularities along the EMP propagation
49 path. The role of linear dispersion and linear absorption leading to the spreading of the UWB
50 EMP and a decrease in its amplitude has been extensively studied (see (Arnush, 1975;
51 Cartwright & Oughstun, 2009; Dvorak, et al, 1997) and references therein), as well as nonlinear
52 effects for high-power EMPs (Golubev, et al, 2000). Laboratory simulations of UWB EMP
53 propagation in ionosphere are also being developed under the support of analytical and
54 numerical models (Es'kin, et al, 2023; Goykhman et al., 2022; Zudin et al., 2024). However, the
55 effects of ionospheric irregularities on the propagation of UWB EMPs have not been explicitly
56 studied yet, to our knowledge.

57   Generally, the effect of ionospheric irregularities on the propagation of very-high (VHF,
58   30 – 300 MHz), ultra-high (UHF, 300 MHz – 3 GHz), and super-high frequencies (SHF, 3 – 30
59   GHz) that overlap the UWB EMPs' frequency spectrum has been actively studied since the
60   1970s (Perkins, 1975). In recent years, interest in this problem is driven first of all by ensuring
61   the high accuracy of Global Navigation Satellite Systems (GNSS) that use L-band transmission
62   channels (see (Aol et al, 2020; Hong et al., 2020; Mrak et al, 2023; Wernik et al, 2003) and
63   references therein). To date, models of diffraction and scattering on natural ionospheric
64   irregularities with sizes from several kilometers to several meters have been developed that
65   allow one to estimate the amplitude and phase scintillations of monochromatic or narrowband
66   signals (Carrano et al, 2011; Deshpande et al, 2014; Galiègue et al 2017). These models,
67   however, cannot be explicitly applied to analyze the waveforms of UWB EMPs propagating in
68   disturbed ionosphere.

69   Artificial ionospheric irregularities (AIIs) are a manifestation of artificial ionospheric
70   turbulence (AIT) which develops in ionosphere exposed to powerful radio waves (see (Streltsov
71   et al., 2018) and references therein). Generation of AIIs and their effect on the propagation of
72   VHF waves were discovered in early experiments on ionosphere modification (Fialer, 1974).
73   Ground-based HF ionosphere heating facilities located at different geographic latitudes (SURA,
74   Russia; HAARP, USA; EISCAT-Heating, Norway) (Streltsov et al., 2018) are capable of generating
75   the AIIs.

76   In scattering of high-frequency waves, the irregularities with scales from meters (and
77   even decimeters) to kilometers provide dominating impact. Properties of such AIIs were studied
78   in sufficient detail from radar scattering after plasma modification by heating facilities, as well
79   as from the characteristics of artificial radio emission from ionosphere (Dhillon & Robinson,
80   2005; L. Erukhimov et al, 1988; L. M. Erukhimov & Mityakov, 1989; Franz et al, 1999; Frolov et
81   al, 1997; Grach et al, 2016). Direct measurements of AIIs are complicated, however they were
82   performed in rocket experiment (Kelley et al., 1995). A simplified model of AII system can be
83   represented as multiple plasma density depletions up to 10-20% from the background (or
84   "striations") oriented parallel to the geomagnetic field, (Franz et al., 1999; Kelley et al., 1995).
85   Owing to the pronounced anisotropic mobility of electrons and ions in the geomagnetic field,
86   AIIs have nearly cylindrical shape. Axial AII scale $l_\parallel$ is limited by the thickness of the turbulence
87   area and can be as large as several tens of km. Transverse scale of the irregularities $l_\perp$ can be
88   about 10 m or even less. Aspect ratio of irregularities $l_\parallel/l_\perp$ can be of the order of the ratio of
89   frequency of electron collisions with neutral particles to electron gyrofrequency, which
90   amounts 10^{-4} in ionospheric F-layer (Robinson, 2002).

91   Our interest in the effect of AIIs on the propagation of EMPs in the GHz frequency range
92   is because such irregularities can be excited under controlled conditions and be quite small-
93   scaled, i.e. of the order of 10 m or less causing considerable scattering of short (meter and
94   decimeter) waves. Therefore, the developed models of UWB EMP scattering on ionospheric
95   irregularities can in future be verified in active experiments with heating facilities. To date, AII-
96   caused scintillation of L-band signals has been observed using HAARP (Mahmoudian et al.,
97   2018) and EISCAT (Sato et al, 2021) heaters. Moreover, the possibility of generating AIIs of very
98   small transverse scales of the order of 10 cm, or so-called "super small-scale" (SSS) irregularities
99   in the heating experiments is being discussed (Milikh et al, 2008). If density variations in SSS

100 irregularities reach 20-30% (Najmi et al., 2014), such AIIs can in principle lead to strong
101 scattering of GHz signals including UWB EMPs.

102   The frequencies of sub GHz and GHz waves significantly (by several orders of
103 magnitude) exceed the plasma frequency of the F-layer which is typically below 10 MHz, and
104 electron collision frequencies (Soldatov & Terekhin, 2016). This leads to a number of
105 assumptions in a model of UWB EMP interaction with ionospheric irregularities: (1)
106 approximation of collisionless plasma can be used; (2) the influence of geomagnetic field on the
107 EMP dispersion can be neglected. Thus, plasma acts as a medium that is transparent to
108 radiation and does not absorb electromagnetic energy, with an isotropic dielectric constant and
109 a refractive index close to unity. The irregularities manifest themselves as refractive index
110 variations (Hunsucker & Hargreaves, 2007), while scattering of GHz waves is determined by the
111 geometry of irregularities exclusively, i.e. their depth and statistics. However, the three-
112 dimensional geometry of striations turns out to be quite complex, which complicates
113 achievement of analytical solutions.

114   To simulate the propagation of GHz waves in ionosphere in the presence of AIIs
115 numerically, a parabolic wave equation (PWE) is used in combination with a series of phase
116 screens (PSs) that carry information about random distribution of refractive index along the
117 propagation path. Note that similar numerical approach is widely used to assess the effects of
118 atmospheric turbulence on electromagnetic wave propagation (Deshpande et al., 2014; Knepp,
119 2005). Given the limited performance of machine calculations in ionospheric research, two-
120 dimensional PWE in combination with multiple one-dimensional PSs was previously used to
121 estimate ionospheric scintillations (Carrano et al., 2011). Due to low dimensionality of the
122 method, the interpretation and applicability of the results was limited. To represent a realistic
123 geometry in the case when the EMP propagation path through the ionosphere is several
124 hundred kilometers and the AIIs are obviously three-dimensional, it was proposed to use a
125 three-dimensional PWE in combination with a series of two-dimensional PSs (Galiègue et al.,
126 2017), which made it possible to refine the solution at the cost of significant increase of the
127 calculation time.

128   A good alternative are statistical numerical methods like Monte Carlo (MC) technique
129 which are actively employed in the wave propagation and energy transport problems. Monte
130 Carlo method is based on repeated simulation of random ray trajectories and subsequent
131 statistical processing and analysis of the results obtained. This method is used in various fields
132 of atmospheric (Marchuk et al., 2013) and ionospheric (Kim, Yoon, Lee, Pullen, & Weed, 2017;
133 Mountcastle & Martin, 2002; Schlegel, 1973) physics, optics of ocean (Leathers et al, 2004; A.
134 Luchinin & Kirillin, 2017) and biological tissues (Kirillin et al, 2014; Yan & Fang, 2020). When
135 applied to the problems of propagation of electromagnetic waves in randomly inhomogeneous
136 media, the Monte Carlo method allows one to estimate the characteristics of signal amplitudes
137 and phases after their scattering and absorption in a volume with random dielectric
138 irregularities. Random medium can be defined by a set of irregularities with known sizes and
139 refractive index variations, as well as by spatially distributed statistical characteristics of
140 scattering and absorption. Flexibility in setting the medium properties provides an advantage
141 for MC technique compared to analytical and semi-analytical modeling that requires
142 information about the spectral correlation characteristics of the medium which is often

143 available only empirically. Another important point is that MC technique is successfully used to
144 solve problems of propagation of ultrashort (similarly, UWB) pulses in randomly
145 inhomogeneous media (A. G. Luchinin et al, 2019; A. G. Luchinin & Kirillin, 2021; A. G. Luchinin
146 et al, 2024; Sergeeva, Kirillin, & Priezzhev, 2006).

147 The aim of the current paper is to present a methodology based on the Monte Carlo
148 technique for modeling the propagation of a nanosecond EMP in the ionospheric plasma
149 allowing to account for both the dispersion of the EMP in plasma and the effects associated
150 with scattering on small-scaled field-aligned ionospheric plasma irregularities.

151

2 Model description

152

2.1 UWB EMP and ionospheric plasma model

153

154 Let us consider a plane linearly polarized electromagnetic wave with an electric field
155 $E_0(\tau = t - z/c)$ which propagates downwards along vertical direction coinciding the z axis
156 through a plasma layer of total thickness Z_{layer}, where c is the speed of light in vacuum. We
157 assume the nanosecond EMP of duration τ_0 is generated at the top of the layer in the plane z =
158 0 and has a bipolar shape (Soldatov & Terekhin, 2016):

$$E_0(\tau) = H(\eta)H(1-\eta)\eta(\eta - 0.5)(\eta - 1) \tag{1}$$

160 where $\eta = \tau/\tau_0$ and $H(\eta)$ is the Heaviside step function. In frequency domain, the
161 shape of the initial EMP is characterized by spectrum $\tilde{E}_0(f)$:

$$\tilde{E}_0(f) = \int_{-\infty}^{\infty} E_0(\tau)\exp(-j2\pi f\tau)\, d\tau. \tag{2}$$

163 Complex amplitude $\tilde{E}(f, z)$ of the signal harmonic the with the frequency f depends on
164 the pathlength z in uniform plasma as follows:

$$\tilde{E}(f,z) = \tilde{E}_0(f)exp\left(j\frac{z}{c}(1 - n(f))\right), \tag{3}$$

165 where

$$n(f) = \sqrt{1 - f_p^2/f^2} \tag{4}$$

167 is the refractive index in plasma with linear plasma frequency f_p. The latter is defined in

168 CGS metric system as $f_p = \sqrt{\frac{\rho_e e^2}{\pi m_e}}$ where e and m_e are the electron charge and mass,

169 respectively, and ρ_e is the electron density (number of electrons per cm³) in uniform plasma.

170 We suppose the frequency spectrum of a nanosecond EMP propagating in ionosphere
171 belongs to the range from tens MHz to several GHz. For frequencies exceeding the plasma
172 frequency of the F-layer, we neglect the effects of collisions and typical features of wave
173 propagation in the ionosphere located in the geomagnetic field such as the splitting of the
174 dielectric constant for O-mode and X-mode, reflection of waves and their thermal dissipation.

175   Figure 1 shows the evolution of EMP shape after its propagation in uniform plasma layer
176 with thickness of Z_{layer} = 30 km and plasma frequency f_p = 5 MHz calculated using Eq. (3), as
177 well as the its spectrum. Due to dispersion, the shape of UWB EMP undergoes significant
178 changes including shape distortion and considerable center of mass displacement. Pulse center
179 of mass delay $\langle \tau \rangle$ and pulse width $\Delta \tau$ can be estimated numerically as:

$$\langle \tau \rangle = \int_0^\infty E^2(\tau)\tau d\tau \Big/ \int_0^\infty E^2(\tau)d\tau, \tag{5}$$

$$\Delta \tau = \sqrt{\int_0^\infty E^2(\tau)\tau^2 d\tau \Big/ \int_0^\infty E^2(\tau)d\tau - \langle \tau \rangle^2}. \tag{6}$$

180   For propagation in free space the pulse characteristics are $\langle \tau \rangle = 0.5\tau_0$ and $\Delta \tau \cong$
181 $0.29\tau_0$. Note that even in the absence of AIIs, dispersion along the path leads to an increase of
182 the pulse delay and width by more than 10 times.

183   We consider the main effect of the pulse-plasma interaction associated with AIIs and
184 causing difference from propagation in uniform plasma consists in linear scattering of the
185 harmonics as they pass through the refractive index irregularities. We characterize the AIIs by
186 reduced electron density $\rho_{e,str} = \rho_e(1-\delta)$, where $0 < \delta < 1$ is the relative density
187 depletion within the irregularity. For each harmonic f of the EMP the refractive index n_{str} inside
188 the irregularity can be achieved in the following form:

$$n_{str}(f) = \sqrt{1 - f_p^2(1-\delta)/f^2}, \tag{7}$$

190 and meets the condition $n(f) < n_{str}(f) < 1$. Refractive index irregularities due to electron
191 density depletion within AIIs lead to the EMP scattering, and, consequently, to the additional
192 modification of its shape which will be analyzed further within the framework of Monte Carlo
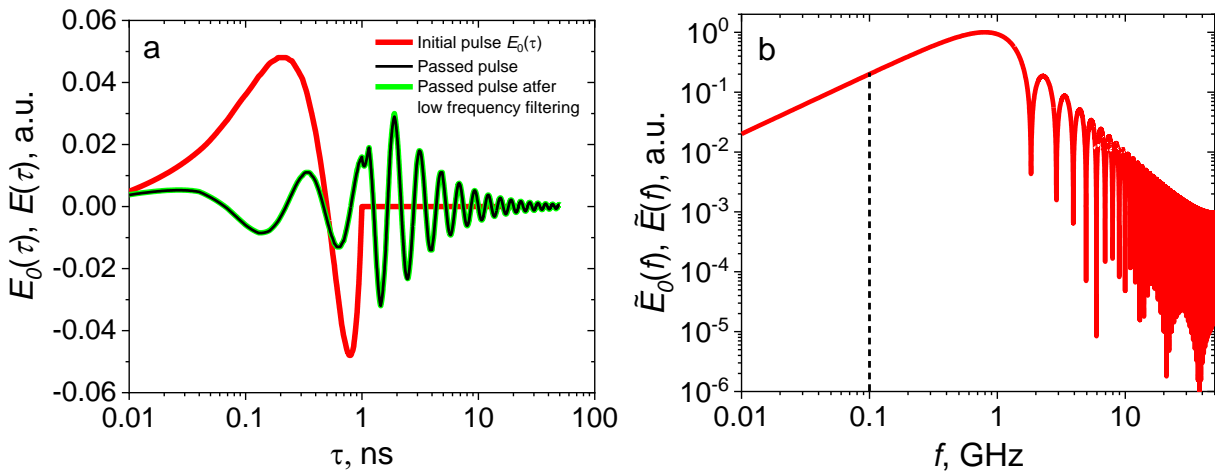193 simulation.

194

195

196   **Figure 1**. Shape of initial bipolar UWB EMP with duration of τ_0 = 1 ns calculated by Eq.(1) and its
197   profile after propagation within a uniform plasma layer of the thickness of 30 km with plasma
198   frequency f_p = 5 MHz as well as the passed pulse profile after filtering the frequencies below
199   100 MHz (**a**); amplitudes of frequency spectrum of initial pulse (**b**).

200   2.2 Monte Carlo technique for modeling the UWB EMP propagation in ionospheric
201   plasma with irregularities

202   Among methods that analyze propagation of electromagnetic radiation in a random
203   medium, Monte Carlo technique implements the principle of wave-particle duality. A wave is
204   presented as a bundle of rays where each ray defines propagation of a small section of the
205   wave front. Random trajectory of each ray is simulated as a set of adjacent piecewise linear
206   sections. The nodes at the connections of these sections are the points of the ray interaction
207   with the scatterers. To consider the wave phenomena, each ray is assigned with the wave
208   attributes, such as amplitude and phase, which vary depending on the particular ray trajectory
209   in the medium.

210   2.2.1 Frequency domain approach

211   One of the advantages of Monte Carlo method in the problem of UWB EMP propagation
212   in ionospheric plasma is its ability to evaluate the effect of AIIs in a certain plasma layer on the
213   scattering of the ray. In radiation transfer problems, Monte Carlo method can be implemented
214   using one of the two most general schemes: (1) a classical scheme with random arrangement of
215   scatterers when all scattering events are considered independent, and the position of each
216   scatterer is determined at each step based on a priori given scattering and absorption
217   parameters of the medium, and (2) a so-called "fixed particle Monte Carlo" (Xiong et al., 2005)
218   in which the positions of the scatterers in the medium are defined in advance.

219   In the first scheme, the result of calculation is the average over various possible
220   ensembles of scatterers, while the second scheme makes it possible to account for the
221   characteristics of radiation propagation within the mean free path in a particular ensemble of
222   scatterers. In this study, we used the first classical approach which allows one to obtain a result
223   averaged over various ensembles leading to a more general solution compared to a particular
224   solution obtained within the second approach.

225   Let us consider the implementation of Monte Carlo algorithm for modeling the ray
226   trajectory of k-th harmonic f_k from the EMP spectrum defined by Eq. (2) in a layer of
227   ionospheric plasma in the presence of AIIs. Geomagnetic field aligned cylindrical striations (see
228   Fig.2) are considered as a statistical ensemble of scatterers. For simplicity all irregularities are
229   assumed to be of the same size but with a varying in-between distance. The input parameters
230   for modeling are the harmonic frequency f_k, plasma frequency f_p corresponding to the average
231   electron density value in the plasma layer, radius r of a single irregularity, mean ray free path
232   (RFP) $\langle l \rangle$ between two adjacent irregularities, depth δ of relative electron density depletions
233   within the irregularity, and thickness Z_{layer} of plasma layer containing striations. The properties
234   of EMP after passing the plasma layer with striations are analyzed at the layer lower boundary
235   $z = Z_{layer}$, which is called "detector plane". Detection area is divided into segments with

236 center position (x_a, y_b) and size $\Delta x \times \Delta y$ where Δx and Δy are dimensions along the
237 corresponding axes.

238 Calculation is based on consequent tracking of N rays which travel from the origin
239 through the plasma layer. Let *i*-th ray ($i = 1...N$) corresponding to the harmonic with frequency
240 f_k be assigned with a local scalar field:

$$E_{i,k}(x, y, z, \tau) = E_{0,k} cos\big(2\pi f_k(\tau + z/c) + \varphi_{0,k} - \phi_{i,k}\big), \tag{8}$$

242 where $E_{0,k}$ and $\varphi_{0,k}$ are, respectively, the field amplitude and initial phase of the harmonic in
243 the plane $z = 0$, and $\phi_{i,k} = \phi_{i,k}(x, y, z)$ is the phase shift along the pathway in dependence on
244 Cartesian coordinates. Local propagation direction is defined by three direction cosines
245 $(\gamma_x, \gamma_y, \gamma_z)$. Random RFP between the two consecutive scattering events is calculated in
246 accordance with semi-empirical concept of single scattering described by the Bouger-Lambert-
247 Beer's law. It defines the average intensity $I(z)$ of the non-scattered plane wave after passing
248 the distance z in the scattering and non-absorbing medium as:

$$I(z) = I_0 \exp(-\mu_s z), \tag{9}$$

250 where I_0 is the initial intensity and μ_s is the scattering coefficient of the medium which is the
251 inverse to the mean free path in the medium: $\mu_s = 1/\langle l \rangle$. In this connection, current RFP is
252 calculated as follows:

$$l = -ln(\xi)/\langle l \rangle, \tag{10}$$

254 where ξ is a random value uniformly distributed in the range (0,1].

255 Interaction of the ray with each irregularity is considered within the framework of
256 geometric optics approach under the assumption that the transverse size of the irregularity
257 significantly exceeds the wavelength for all harmonics of a nanosecond EMP, which limits the
258 lowest spectrum frequency. One iteration of a ray tracing cycle includes searching the
259 intersection point of the ray trajectory with a cylinder, calculating reflection coefficient R_{ref} of
260 the ray by the cylinder surface in accordance with the Fresnel law. Occurrence of reflection is
261 defined by the condition:

$$\zeta < R_{ref}, \tag{11}$$

263 where ζ is a random value uniformly distributed in the range (0,1]. If condition (11) is met, the
264 ray direction changes in accordance with the reflection law, and a new RFP in the external
265 medium is generated according to Eq. (10). If condition (11) is violated, refraction of the ray
266 occurs. The ray changes its direction according to the Fresnel law and propagates through the
267 irregularity to its far boundary, where the reflection test using condition (11) is performed
268 again. Simulation of the ray propagation inside the irregularity is performed until a refraction
269 event occurs at the cylinder-plasma boundary and the ray exits into the surrounding plasma. In
270 this case, a new iteration begins by evaluation of the free path using Eq. (10). Iterations are
271 repeated until the ray exits the boundaries of the medium or reaches the detector plane
272 $z = Z_{layer}$ which coincides with the lower boundary of the layer with irregularities. Output
273 coordinates $(x_i^{ex} \; y_i^{ex})$ of the i-th ray in the detection plane are recorded together with the total
274 phase shift $\phi_{i,k}^{ex}$:

275
$$\phi_{i,k}^{\text{ex}} = 2\pi f_k \big(n(f_k)L_{p,i} + n_{str}(f_k)L_{str,i} \big)/c, \tag{12}$$

276 where $L_{p,i}$ is the total ray path in surrounding plasma and $L_{str,i}$ is the total ray path inside
277 irregularities.

278 At the final stage, averaging of field oscillations $E_{i,k}(x^{\text{ex}}, y^{\text{ex}}, \tau) = \tilde{E}_{0,k}(f)\cos(2\pi f_k(\tau +$
279 $Z_{layer}/c) + \varphi_{0,k} - \phi_{i,k}^{\text{ex}})$ of all rays reaching the detector plane $z = Z_{layer}$ within the segment
280 (x_a, y_b) is performed:

281
$$E_k^{ray}(x_a, y_b, \tau) = \sum_{i|x_a < x_i^{\text{ex}} < x_a + \Delta x, y_b < y_i^{\text{ex}} < y_b + \Delta y} E_{i,k}(x_i^{ex}, y_i^{ex}, Z_{layer}, \tau) \ /N. \tag{13}$$

282 It is assumed in Eq. (13) that the output direction of the ray does not change significantly with
283 respect to the initial direction.

2.2.2 Frequency scattering map construction

285 To analyze the structure of the EMP in space and time, it is convenient to present the
286 pulse by a discrete Fourier spectrum with a set of harmonics $f_k = k/T$ (k = 1...N_k):

287
$$\tilde{E}_{0,k} = \frac{1}{T} \int_0^T E_0(\tau)\exp(-j2\pi f_k \tau)\, d\tau, \tag{14}$$

288 where T is the pulse record time. Previously described Monte Carlo simulation of ray
289 propagation can be then performed for each harmonic f_k followed by summation for all
290 harmonics within the detector segment (x_a, y_b):

$$E^{pulse}(x_a, y_b, \tau) =$$

291
$$= \sum_k E_k^{ray}(x_a, y_b, \tau) = \sum_k \sum_{\substack{i|x_a < x_i^{\text{ex}} < x_a + \Delta x, \\ y_b < y_i^{\text{ex}} < y_b + \Delta y}} E_{0,i}^k \cos\big(2\pi f_k(\tau + Z_{layer}/c) + \varphi_{0,k} - \phi_{i,k}^{\text{ex}}\big). \tag{15}$$

292 For better visual representation of both effects of scattering and dispersion on the EMP
293 propagation we propose to construct "frequency scattering maps" similar to construction of a
294 point spread function. These maps illustrate the deviations of particular frequency harmonics
295 from straight forward propagation due to scattering, and their arrival to a particular detector
296 segment (x_a, y_b). Such maps can provide a complete picture of the scattering role in ray
297 deflecting from the straight forward propagation. We constructed the 2D map of minimal D_f^{min}
298 and maximal D_f^{max} nonzero frequencies of the pulse discrete spectrum $\tilde{E}$:

299
$$D_f^{min}(x_a, y_b) = \min(\ f_k | \tilde{E}(x_a, y_b, f_k) > 0) \tag{16}$$

300
$$D_f^{max}(x_a, y_b) = \max(\ f_k | \tilde{E}(x_a, y_b, f_k) > 0) \tag{17}$$

301 To our knowledge, it is the first example of this approach in the analysis of spatial-spectral
302 structure of EMPs in a plasma medium.

2.2.3 Simulation of plane wave

304 When the source is located at a fairly large distance from the ionospheric layer (significantly
305 exceeding its thickness), the problem can be considered in the plane wave approximation. It
306 means that electric field is transversely uniform in the plane of the layer boundary and the

307 solution obtained for a single ray can be averaged over the detection plane. The solution for a
308 plane wave can be obtained as follows:

$$E^{planar}(\tau) = \sum_{a,b} E^{pulse}(x_a, y_b, \tau) =$$

309
$$= \sum_{a,b} \sum_k \sum_{i|x_a<x_i^{ex}<x_a+\Delta x,} E_{0,i}^k \cos\left(2\pi f_k\left(\tau + Z_{layer}/c\right) + \varphi_{0,k} - \phi_{i,k}^{ex}\right). \qquad (18)$$
$$y_b<y_i^{ex}<y_b+\Delta y$$

310 In the case of modeling a spherical wave, the effect of the shape of the spherical front can be
311 accounted by modeling a set of rays with individual initial directions, initial phase shift and
312 coordinates of the entry point into the layer based on an a priori given position of the source.
313 Modeling with such initial parameters is carried out separately for each harmonic.

314   2.3   Problem statement

315   In this study, we considered propagation of an EMP in a layer of ionospheric plasma of
316 thickness of Z_{layer} = 30 km containing cylindrical irregularities with radius of r = 10 m (Kelley et
317 al., 1995) oriented at an angle of $\alpha = 18^o$ relative to vertical direction which mimic striations
318 formed under mid-latitude ionospheric heating conditions as in experiments with SURA heating
319 facility. Average RFP between the irregularities was chosen as $\langle l \rangle$ = 30 m. Relative depth of
320 electron density depletions within striations varied in the range of δ = 5% - 50%. The largest
321 values of δ are hardly realistic, and used in simulations in demonstrative purposes only. Two
322 values of electron density in unperturbed plasma were considered corresponding to plasma
323 frequencies f_p = 5 MHz and 10 MHz. The pulse duration τ_0 was assumed to be equal to 1 ns, its
324 initial profile in the plane z = 0 was given by Eq.(1). Typical trajectory of a ray propagating in the
325 layer with the cylindrical irregularities is shown in Fig. 2. The number of random ray trajectories
326 used in the simulations for individual harmonics varied in the range of $N = 10^5$-10^6. These values
327 were chosen based on preliminary simulations and ensure the invariance of the key
328 observables analyzed in this study, such as pulse delay or pulse width, with respect to the
329 number of trajectories employed in simulations. Detector plane had the size of 4000 m in X
330 direction and 160 m in Y direction, while the size of segments Δx and Δy are 1 m on default, and
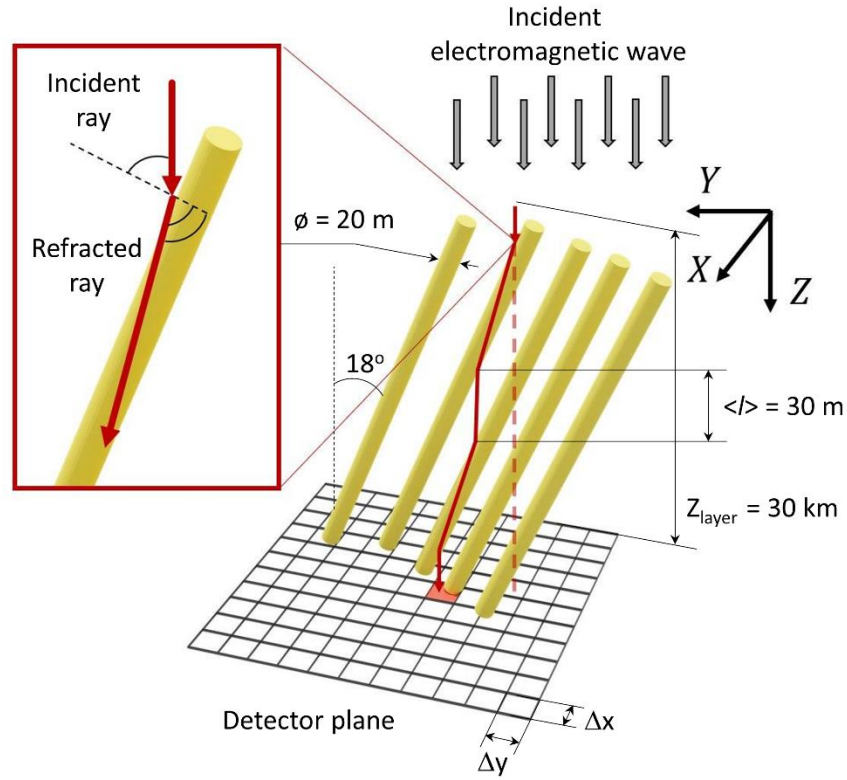331 could be specified differently in separate cases.

Figure. 2. Schematic of the model: typical ray trajectory when scattering on ionospheric irregularities.

3 Simulation results

3.1 Frequency spectrum of a nanosecond pulse in Monte Carlo simulations

First, we have to define the number N_k of discrete Fourier spectrum harmonics employed in Monte Carlo simulations of UWB EMP propagating in plasma with striations according to Eq.(14). The shape of the initial 1-ns pulse given by Eq. (1) is shown in Fig.1 (a) while analytically calculated harmonic spectrum of the initial pulse and the pulse passing a layer of uniform plasma with plasma frequency f_p = 5 MHz are shown in Fig.1(b). Lower frequency limit of 10 MHz is related to the pulse record time of 100 ns, while upper frequency limit of 50 GHz is caused by temporal resolution of the incident pulse which was taken as 10^{-2} ns. Total number of counts used in analytical calculation is $N_{counts} = 10^4$ yielding $N_k = N_{counts}/2 = 5 \cdot 10^3$ harmonics required to compose the pulse.

In Monte Carlo modeling of the ray propagation in plasma with striations, several assumptions are made which put certain restrictions on the harmonic spectrum of the pulse. First, the transverse scale of striations is assumed large compared to the particular harmonic wavelength so that ray optics can be employed. In the case r = 10 m this condition is met for frequencies not less than 100 MHz which means the first 10 harmonics in the range of 10-100

351   MHz should be withdrawn from the EMP spectrum. Fig.1(a) demonstrates the effect of low-
352   frequency filtering on the distortion of the passed pulse shape. The effect is rather minor and it
353   is almost negligible in the main body of the pulse in the range of 1-10 ns since the relative loss
354   of energy due to the withdrawn harmonics is below 0.2%. Another restriction comes from large
355   number of harmonics needed to be simulated for correct reconstruction of a scattered pulse
356   shape, which leads to intensive Monte Carlo modeling. In sub-GHz and GHz range the effect of
357   the ray refraction is mostly pronounced for lower harmonics while higher harmonics experience
358   less refraction. The question is in defining the domain of higher harmonics for which phase
359   delay can be evaluated analytically avoiding time-consuming Monte Carlo tracing.

360   3.2 Ray trajectories for different frequency harmonics

361   We considered tracing a single pulsed ray incident on a 30-km-thick layer of plasma in
362   the origin (x = 0, y = 0, z = 0) and directed along Z axis. We simulated the ray propagation in the
363   plasma layer with plasma frequency f_p = 5 MHz containing density irregularities with δ = 15%
364   which corresponds to some observations (Kelley et al., 1995), as well as the layer with plasma
365   frequency f_p = 10 MHz with the irregularities with δ = 50% which is beyond natural conditions
366   and is presented as a limiting case. Fig. 3 demonstrates normalized statistical distribution of ray
367   pathlengths in plasma (L_p) and in striations (L_{str}) registered in the whole detector plane
368    $z = Z_{layer}$ for four individual EPM harmonics with frequencies of 0.1 GHz, 0.3 GHz, 1 GHz and
369   50 GHz. In the case of small δ (Fig. 3a) all distributions are Gaussian-shaped with peak position
370   and width depending on the harmonic frequency. Lower harmonics are characterized by
371   smaller pathlengths in plasma and larger pathlengths within irregularities, as well as by
372   narrower width of the distribution. In the case of large f_p and δ (Fig. 3b) the pathlength
373   distribution function is asymmetric for lowest harmonics with noticeable contribution of large
374   pathlengths both in striations and in the surrounding plasma which describes wandering of the
375   ray due to multiple refractions. Dependence of average pathlengths $\langle L_p \rangle$ and $\langle L_{str} \rangle$ on the
376   frequency for both cases of (f_p, δ) is plotted in Fig. 4 for eight harmonics within the range 0.1 –
377   50 GHz. Average pathlength increases in plasma with the harmonic frequency (Fig. 4a) while it
378   decreases within striations (Fig. 4b) thus showing the lowering effect of refraction in higher
379   harmonics. The curves $\langle L_p \rangle$ and $\langle L_{str} \rangle$ are almost identical for both cases of (f_p, δ) except for
380   the region of smallest frequencies where the effect of large-path tail in the distribution for f_p =
381   10 MHz and δ = 50% is evident. Asymptotic average pathlength at high frequencies is almost
382   the same for weak and strong electron density depletions and amounts about $\langle L_p \rangle$ = 12.4 km
383   and $\langle L_{str} \rangle$ = 17.6 km while their sum is equal to the layer thickness Z_{layer}=30 km.
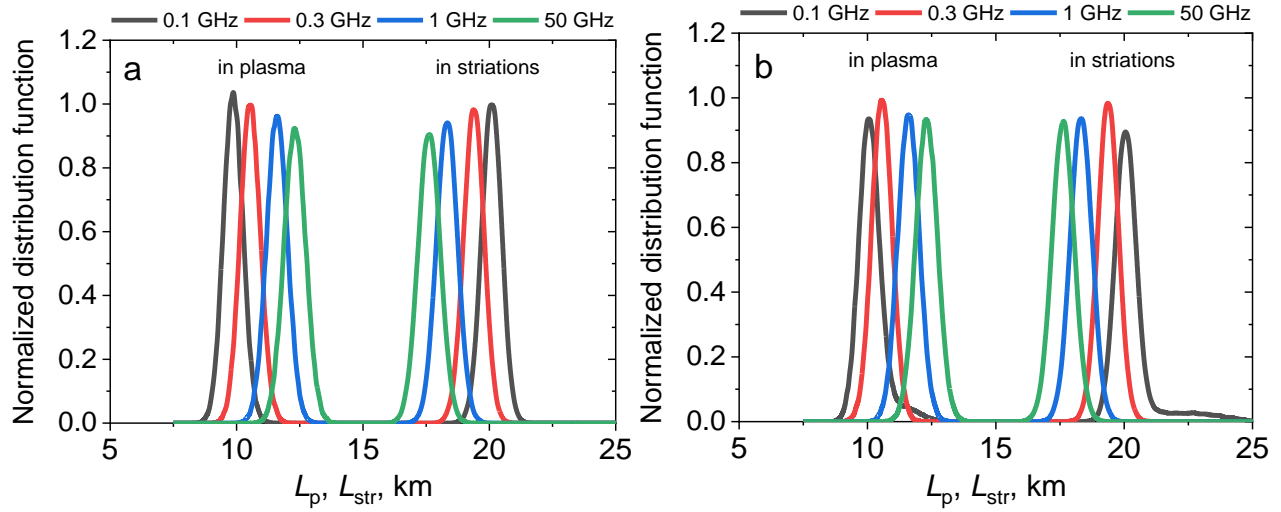
384

Figure. 3. Normalized distributions of total pathlength within plasma and striations of the EMP harmonics with the indicated frequencies for the parameters f_p = 5 MHz, δ = 15% (**a**) and f_p = 10 MHz, δ = 50% (**b**).
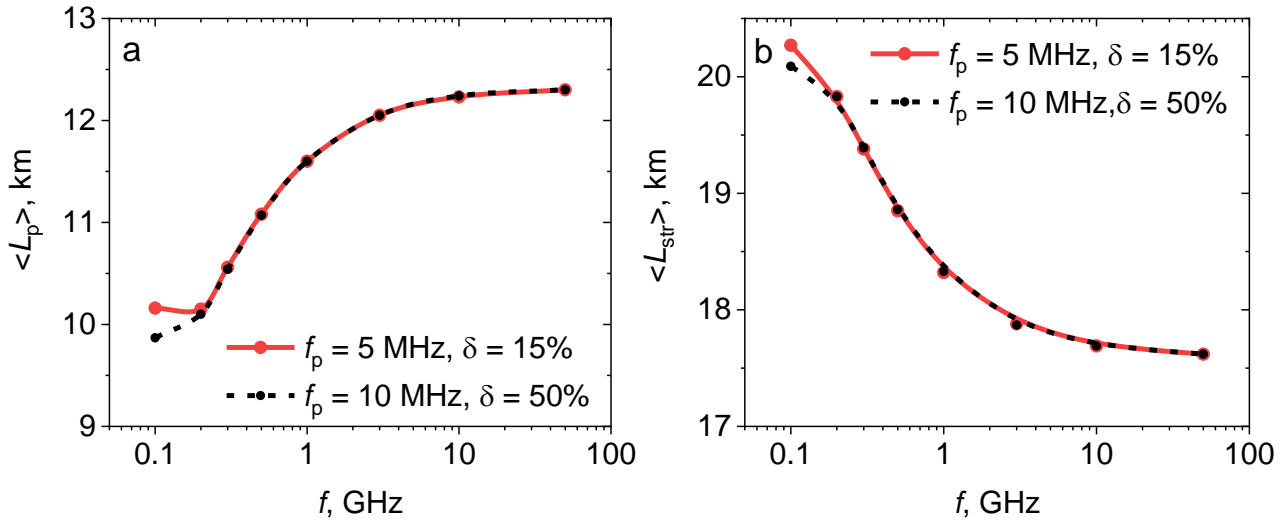

388

Figure. 4. Average pathlength within background plasma (**a**) and striations (**b**) versus frequency for the parameters f_p = 5 MHz, δ = 15% (a) and f_p = 10 MHz, δ = 50% (b).

391

In Fig. 5 scattering maps of minimum D_f^{min} (Fig. 5a) and maximum D_f^{max} (Fig. 3b) frequencies from the UWB EMP discrete spectrum are shown. Spatial resolution in the maps is Δx = Δy = 1 m both in the direction parallel to the projection of the cylinder axis onto the detector plane (Y axis), and orthogonal to it (X axis). The brightest spot in both maps covers central segment around (0, 0, Z_{layer}) point of the detector plane in which all the harmonics of the non-refracted pulse should be observed. In the case of random refraction, lower frequencies deviate from straightforward propagation. The largest shift takes place for smallest

399   frequencies in the spectrum which is related to the maximum difference in the refractive

400   indices n and n_{str} (see Eq.(4) and Eq.(7)). The anisotropy of the frequency distribution is due to

401   the inclination of the irregularities at the angle of $\alpha = 18^\circ$ with respect to vertical direction.

402   Non-uniform displacement is observed along Y axis, i.e., in the direction parallel to the

403   projection of the cylinder onto the detector plane, while in the orthogonal direction (along X)

404   the distribution is symmetric due to random positions of the striations relative to the initial

405   beam direction.

406   The D_f^{min} map (Fig. 5a) shows that all harmonics with frequencies less than 0.3 GHz

407   experience a shift in Y direction, and, hence, the signal in the central segment of the detector,

408   associated with the part of the pulse which passes through the medium without scattering, is

409   composed of higher harmonics. The entire scattering region for all harmonics covers the range

410   of ±500 m along X-axis and less than 20 m along Y-axis. According to Fig. 5b, the highest

411   harmonics deviate within the limits of one segment along Y direction with size of 1 m, and

412   within ±20 m along X axis.

413

414
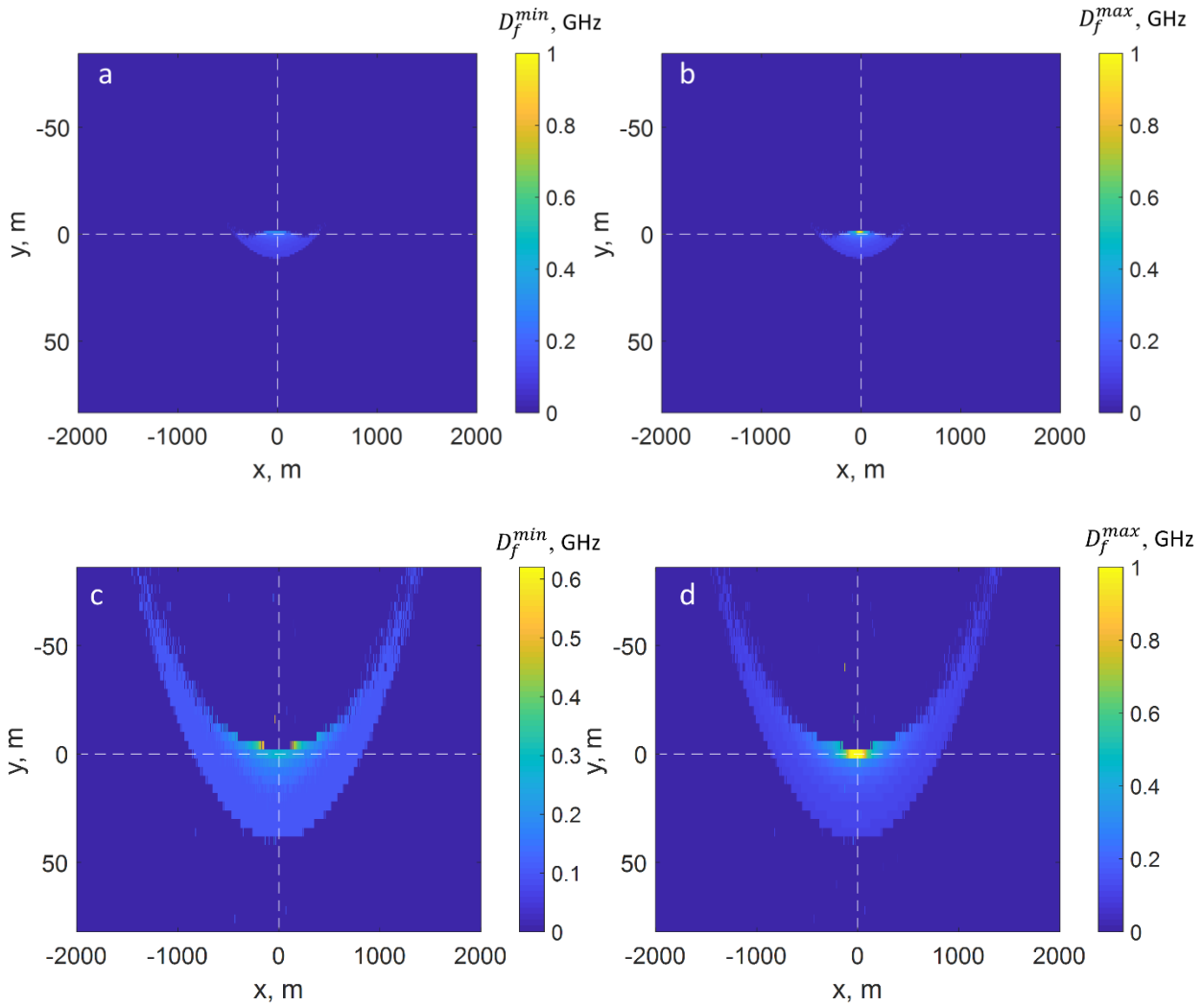
415 **Figure 5.** Scattering maps of minimum D_f^{min} (**a,c**) and maximum D_f^{max} (**b,d**) nonzero harmonics
416 of EMP discrete spectrum detected after propagation within 30-km-thick plasma layer with
417 plasma frequency of f_p = 5 MHz containing AIIs with variation of electron density δ = 15% (**a,b**)
418 and δ = 50% (**c,d**).
419

420   An increase of electron density depletions depth leads to the increased scattering of
421 EMP. Figures 3c,d show frequency scattering maps for the case of δ = 50% corresponding to
422 intense irregularities. Typical size of the scattering region increases up to 120 m along Y
423 direction, and up to ±3000 m in X direction. D_f^{min} map (Fig.5c) shows that higher harmonics (up
424 to 0.6 GHz) experience stronger deviation compared to the case of weaker irregularities, ⍰ =
425 15%, (Fig. 5a) where deviation was observed for frequencies below 0.32 GHz only.

426   Detailed analysis of zoomed-in central parts of D_f^{max} maps (Figs.5b and 5d) shows that
427 maximum frequencies which deviate from the central detector segment of the size 1x1 m^2 are
428 below 10 GHz. This allows limiting the modeling of propagation of different harmonics by
429 frequencies in the range of 100 MHz - 10 GHz with the step of 10 MHz. Phase delay of higher
430 harmonics with frequencies in the range 10-50 GHz propagating in plasma with striations will
431 can be estimated using asymptotic average path lengths $\langle L_p \rangle$ and $\langle L_{str} \rangle$ and asymptotic
432 dispersion relation used in high-frequency approximation (Soldatov & Terekhin, 2016):

433 $$\phi_k^{ex} \cong \frac{2\pi f_k}{c}\left(Z_{\text{layer}} - \frac{f_p^2}{2f_k^2}(\langle L_p \rangle + (1 - \delta)\langle L_{str} \rangle)\right) \qquad (19)$$

434 The number of harmonics in MC simulations can be thus 5 times reduced, from 5000 to less
435 than 1000.

436   3.3 Scattered pulse profiles and characteristics

437   Figure 6 shows the waveforms of partial pulsed signals $E^{pulse}(x, y, \tau)$ detected by
438 different segments of the plane $z = Z_{layer}$. For weaker scattering with δ = 15% the detector
439 segments have size 1x1 m^2 (Fig. 6a-c); for stronger scattering with δ = 50% the segment size is
440 4x4 m^2 (Fig. 6d-f). The waveforms are presented in a central segment of the detector plane
441 (Fig.6a, d) and size 1x1 m^2 (Fig. 4a) and 4x4 m^2 (Fig. 6d) which fully collects the pulse in the case
442 of uniform plasma, as well as by the segments of the same size shifted along X axis at distances
443 of 20 m (Fig. 6b, e) and 40 m (Fig. 6c, f). The waveforms of partial pulses are composed
444 according to Eq.(15) with account for all harmonics arriving at a defined detection segment, and
445 are plotted versus the time variable $\tau = t - Z_{layer}/c$. The figure demonstrates that the pulse
446 waveform detected in the central segment and therefore composed of a large number of
447 harmonics differs considerably from that in the shifted segments where the signal is formed by
448 scattered harmonics at low frequencies predominantly. An attenuation of the signal amplitude
449 as well as the delay of the pulse center of mass are observed with the increase of the
450 transverse shift. Figure 7 presents dependences of the scattered pulse amplitudes
451 $\max(|E^{pulse}(x, y, \tau)|)$ versus the shift along X axis (Fig. 5a) and Y axis (Fig. 7b) for three
452 different values of δ = 15, 30, and 50%. Amplitude decays nearly exponentially in X direction for
453 up to 100 m (Fig. 7a) with the decay rates that decrease with the increase of δ. Slow decay at

454 large distances is most pronounced for high δ and is apparently related to deflection due to
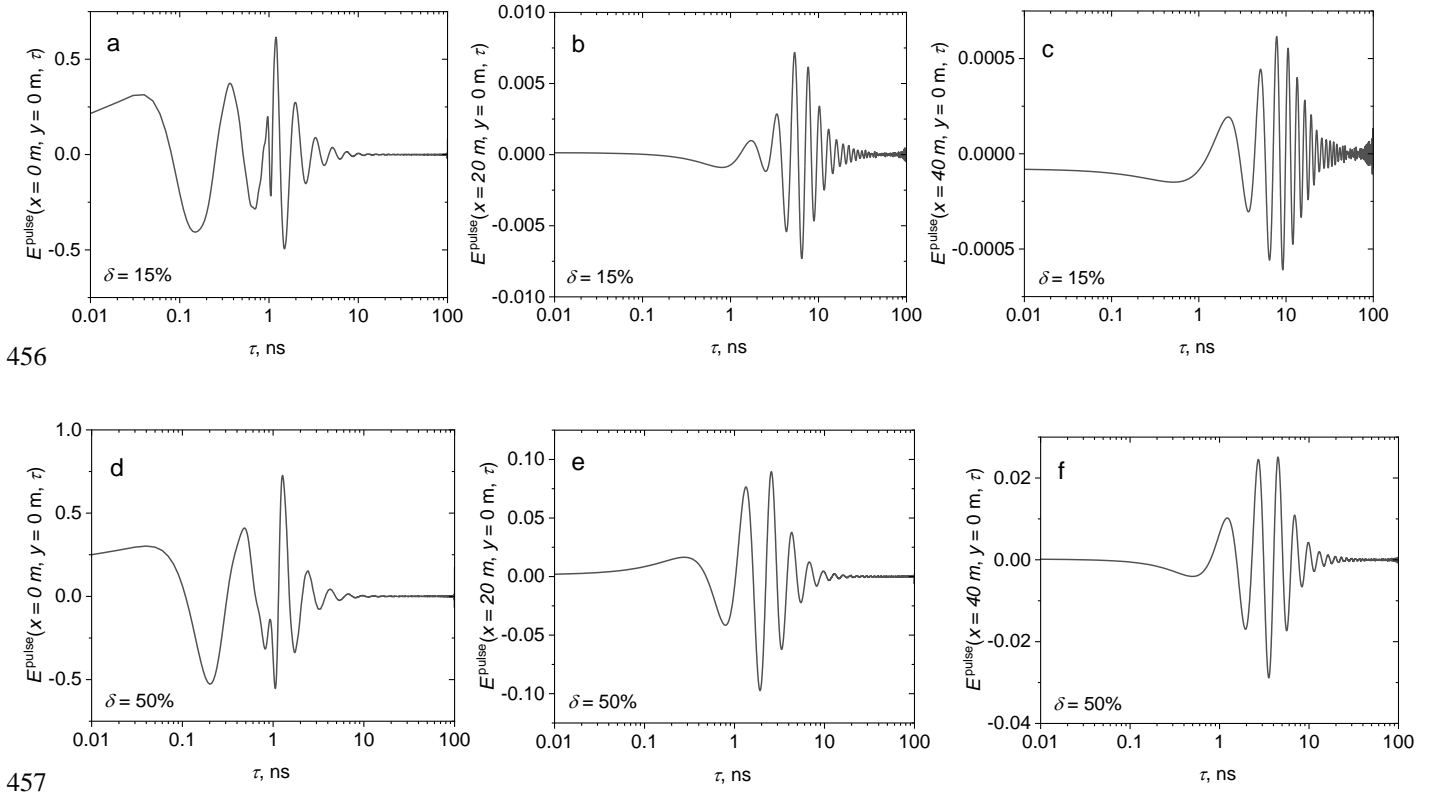455 strong multiple refraction.

456

457

Figure 6. Partial pulses $E^{pulse}(x, y, \tau)$ detected within the central segment (**a,d**) and segments
459 shifted along X axis for 20 m (**b,e**) and 40 m (**c,f**) after the ray propagation in a 30-km-thick
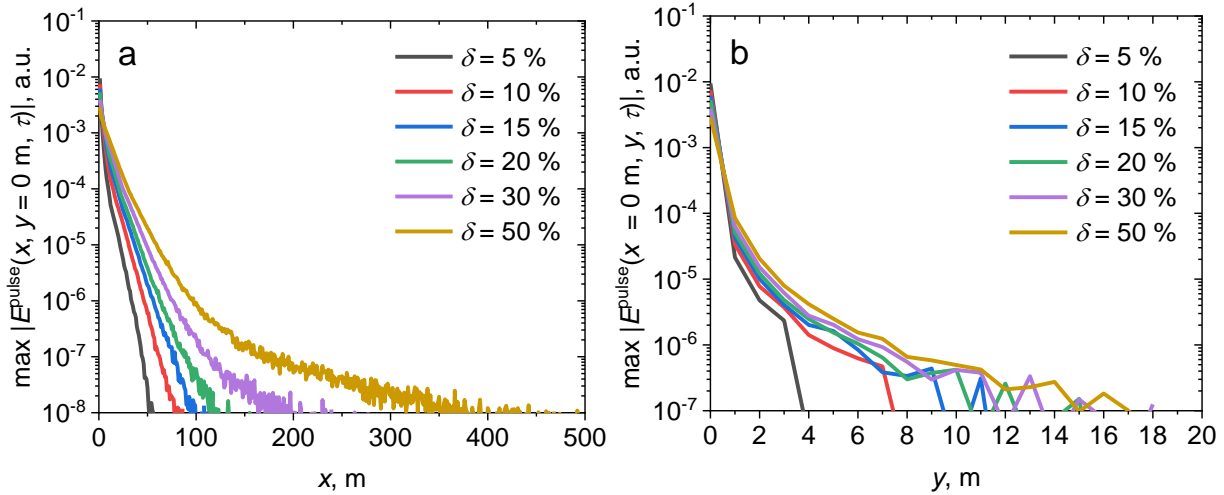460 plasma layer with plasma frequency f_p = 5 MHz in the presence of AIIs with δ = 15% (**a-c**) and δ
461 = 50% (**d-f**).

462

Figure 7. Dependence of the scattered pulse amplitude max ($|E^{pulse}(x,y,\tau)|$) on transversal shift along X axis (**a**) and Y axis (**b**) after propagation in a 30-km-thick plasma layer with plasma frequency f_p = 5 MHz in the presence of AIIs for various values of electron density depletion δ.

Study of average delays of the detected partial pulses is of particular interest. In Fig. 6 maps of average delay of partial pulsed signals $E^{pulse}(x,y,\tau)$ calculated by Eq.(5) are presented for the cases of δ = 15% (Fig. 8a) and δ = 50% (Fig. 8b). Note that in the central part of the detection plane the case of δ = 15% (Fig. 8a) is characterized by larger delay values compared to the case of δ = 50% (Fig. 8b) for a given shift of the detection segment despite stronger scattering in the latter case with larger spreading of detected rays. It should be noted that typical delays are of few ns in the segments close to the central one, and can reach 72 ns at the periphery. A detailed interpretation of this phenomenon will be given in the next section devoted to the simulation of a plane wave propagation.
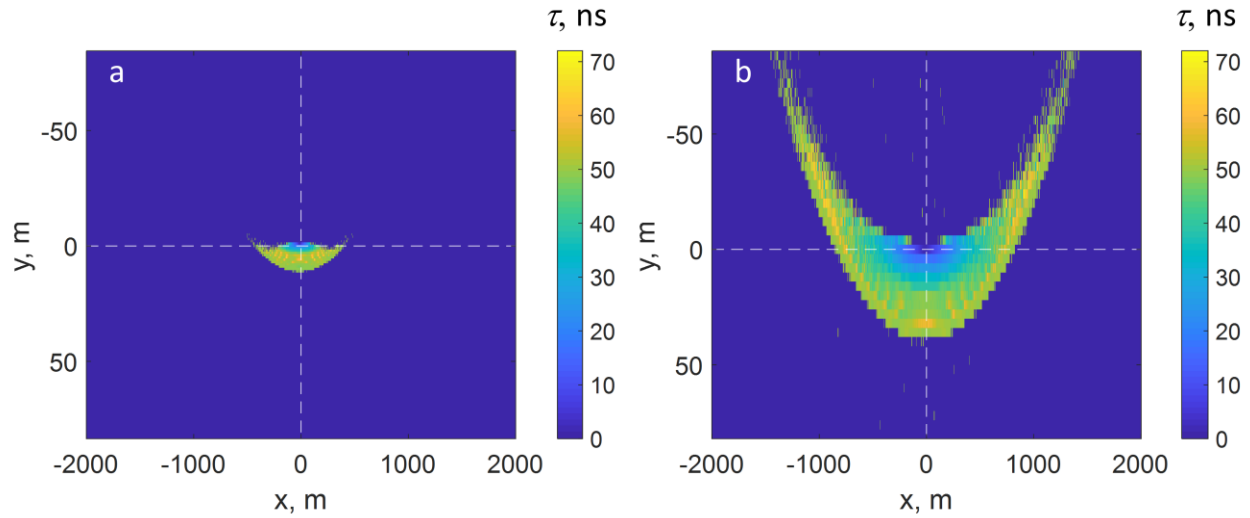
Figure 8. Delay maps of detected partial pulses after the ray propagation in a 30-km-thick plasma layer with plasma frequency f_p = 5 MHz in the presence of AIIs with values of electron density fluctuations δ = 15% (**a**) and δ = 50% (**b**).

3.4 Simulation of the propagation of a nanosecond pulse in the plane wave approximation

To expand the presented results on the case of plane-wave EMP propagation we employ the approach described by Eq.(18). For each harmonic, the electric fields detected within the whole detector plane $z = Z_{layer}$ are summarized and then all harmonics are converted into a pulse. This simplified approach does not account for the effect of polarization change when calculating the net field. Such an assumption was previously made in (Soldatov & Terekhin, 2016) in a high-frequency limit. Being convenient, it yields an approximate pulse structure with overestimated net amplitudes of the harmonics. In our study, the influence of polarization change at the boundaries of striations may be significant for lower frequencies. However,

491 preliminary analysis in the frames of geometrical optics shows that depolarization of radiation
492 (polarization vector rotation for linearly polarized field) due to scattering on irregularities is of
493 the same order as the angular spread of wave vectors θ_k of the rays arriving to the observation
494 point. This statement can be easily verified by considering the incidence of a beam on a flat
495 boundary of two isotropic media. The greatest angle of rotation of the electric field intensity
496 vector will be observed in the case of a TM wave, and it will be equal to the angle of rotation of
497 the wave vector. In the case of a TE wave, the electric field vector will not rotate at all. The
498 magnitude θ_k, in its turn, can be evaluated from scattering maps (Fig.5) as $\Omega_k \approx 0.05$ - 0.1 for
499 lower harmonics. Therefore, the effect of polarization change can be omitted at the current
500 step, while the results obtained under the stated assumption can be considered as a reference
501 for future detailed findings.

502 To demonstrate the effect of random striations on the pulse waveform, we compared
503 two models of electron density distribution with depletion. First model is attributed as "no
504 scattering" where plasma is considered as a uniform medium with an effective refractive index:

$$n_{eff}(f) = \frac{\langle L_p \rangle\, n(f) + \langle L_{str} \rangle\, n_{str}(f)}{Z_{layer}} = \frac{1.24 n(f) + 1.76 n_{str}(f)}{3} \qquad (20)$$

506 Propagation of all the harmonics in such medium is considered straight-forward with the
507 phase shift calculated in accordance with Eq. 15. Another model is attributed as "scattering",
508 and describes the pulse propagation in plasma with cylindrical irregularities simulated by
509 Monte Carlo technique in accordance with Section 2.2.4.

510 The results of modeling the pulse transformation in the plane wave approximation are
511 presented in Fig. 9a-c for background plasma frequency f_p = 5 MHz and different values of δ.
512 For reference, the waveforms of the EMP propagating in uniform plasma (attributed as
513 "uniform plasma") are shown. The presence of irregularities leads to the distortion of the EMP
514 waveform which becomes stronger with the increase of δ It is worth noting that the pulse
515 waveforms in uniform plasma differ from those in plasma with density distortions both for "no
516 scattering" and scattering" cases. The difference between the latter two cases also grows with
517 the increase of δ value, which is most clearly seen from Fig. 9c for δ = 50%.
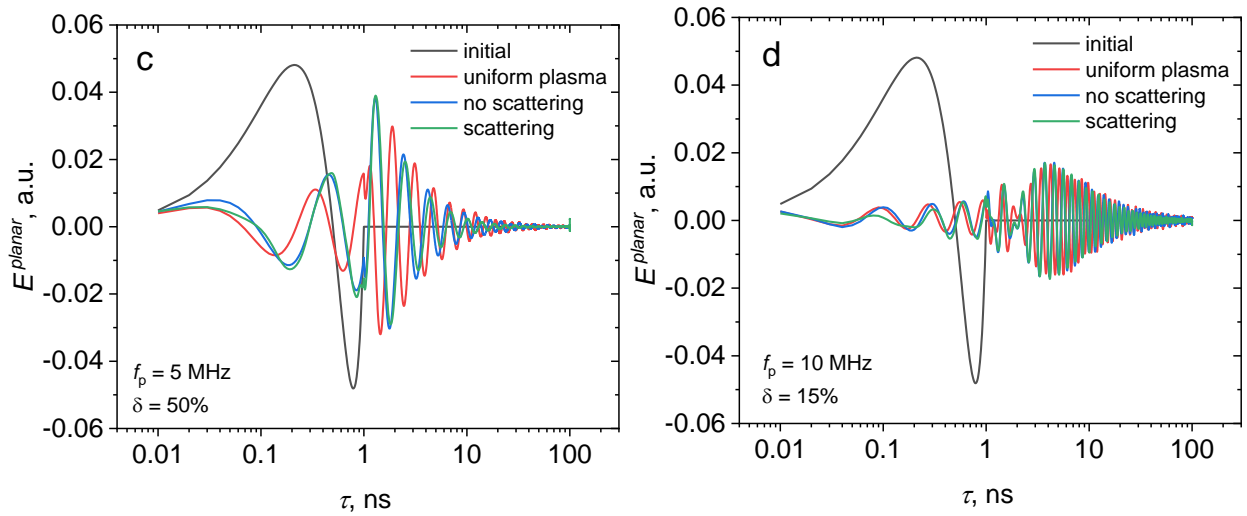

518

519
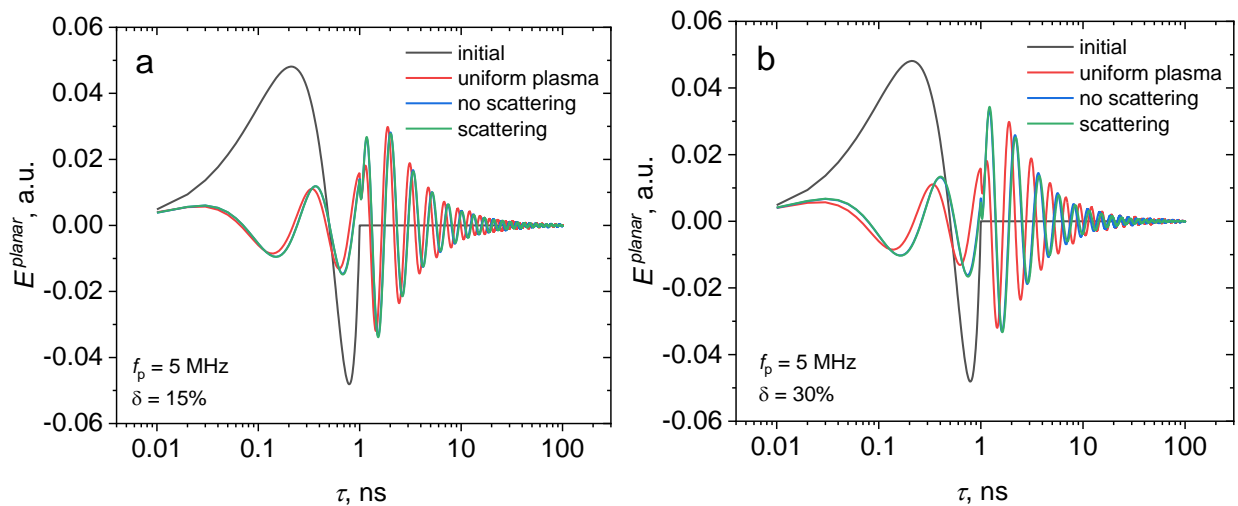
Figure 9. Waveforms of a plane wave EMP $E^{planar}(\tau)$ after propagation in a 30-km-thick plasma layer with background plasma frequency f_p = 5 MHz for uniform plasma ("uniform plasma"), in a medium with effective refractive index depending on electron density fluctuations ("no scattering"), and in plasma with AIIs ("scattering") for electron density fluctuations δ = 15% (**a**), 30% (**b**), 50% (**c**), and δ = 15% with f_p = 10 MHz (**d**). Initial EMP waveform is given as a reference.

Figure 9d shows the results of the EMP waveform simulations for the case of high background plasma frequency f_p = 10 MHz when the refractive index dispersion is more pronounced. This case is manifested by larger overall delays of the pulse body compared to the case of f_p = 5 MHz. As it seen from comparison of the EMP waveforms in Fig.9a and Fig.9d for the same δ but different f_p values, dispersion has greater impact on the pulse shape compared to scattering effects.

The results of calculating the delays of the EMP center of mass by Eq.(5) are presented in Fig. 10a. Starting point of the plot is a relative delay for a pulse in uniform plasma given as a reference and indicated as "δ = 0". The figure shows data for both models of density distributions ("no scattering" and "scattering" cases). In "no scattering" model, a delay of the EMP center of mass decreases with the increase of δ, which is explained by the fact that refractive index n_{str} tends to 1 with the growth of δ. As a result, average refractive index of the medium also becomes closer to 1 resulting in smaller effect of dispersion. What is worth noting is that the presence of scattering additionally reduces the EMP delay. This is expectable for a plasma-type medium with a refractive index below unity since larger propagation paths of scattered waves give an additional phase delay. As a result, larger propagation paths partly compensate the dispersion. This effect is especially pronounced for smaller frequencies, for which the refractive index n is smaller, however, scattering is also stronger. Moreover, scattering seems to play a more significant role in dispersion compensation for larger δ as compared to "no scattering" case. The effect of scattering can also be illustrated by the delay maps (Fig. 8) which show angular spreading due to scattering. Curves for f_p = 5 MHz and f_p = 10 MHz demonstrate similar systematic decrease of $\langle\tau\rangle$ in the presence of irregularities compared

548 to the case of EMP propagation in a uniform plasma with effective refractive index. For higher
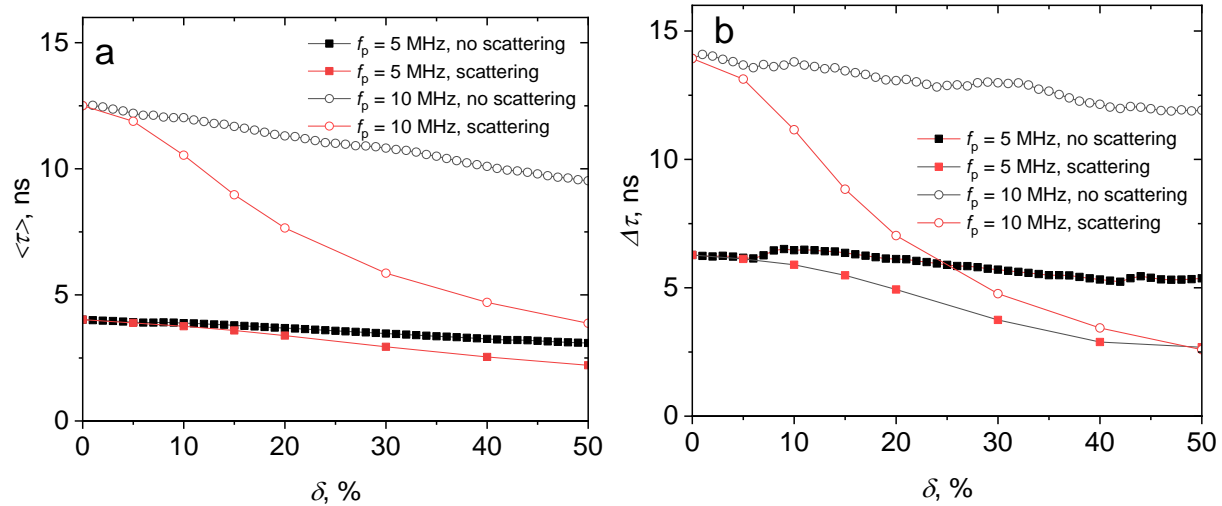549 value of f_p a decrease in $\langle\tau\rangle$ is more apparent.

550
551

552 Fig. 10. Center of mass delay with respect to EMP propagation in free space (**a**) and pulse width
553 of the pulsed plane wave (**b**) scattered in a 30-km-thick plasma layer with background plasma
554 frequencies f_p = 5 and 10 MHz in the presence of AIIs with different values of δ: cases of
555 uniform plasma with effective refractive index (no scattering) and plasma with random
556 cylindrical irregularities (scattering).

557

558 Dependences of the pulse width $\Delta\tau$ versus the value of δ calculated by Eq.(6) are shown
559 in Fig. 10b for both low and high plasma frequencies and demonstrate trends similar to those
560 observed for $\langle\tau\rangle$. This figure also confirms that the presence of the refractive index irregularities
561 can partly compensate dispersion effects and diminish pulse widening. As density depletions
562 become deeper with the growth of δ, scattering plays more significant role in compensation of
563 EMP broadening due to the dispersion.

4 Discussion and Conclusions

565 In this study, a methodology based on the Monte Carlo technique was developed for
566 modeling the linear propagation of a nanosecond electromagnetic pulse (EMP) in ionospheric
567 plasma in the presence of field-aligned depleted density irregularities, which are similar to well-
568 known striations stimulated by HF heating experiments. By employing individual ray tracing
569 approach, this technique allowed to analyze the effect of scattering by the irregularities on
570 lower and higher frequency harmonics of the EMP for different electron densities
571 corresponding to typical plasma frequencies from 5 MHz to 10 MHz. Due to the specific
572 orientation of the irregularities the scattering is anisotropic and is elongated in the direction
573 transversal to irregularities axis projection on the lower boundary of the layer with density
574 irregularities. The harmonics below 0.3 GHz deviate from the initial direction for more than 1 m
575 within a 30-km path, while harmonics above 10 GHz experience almost no deviation. Simulation

576   of a plane wave propagation demonstrated two competing phenomena affecting the structure
577   of the outcoming EMP. On the one hand, the scattering leads to energy loss in the
578   straightforward pulse. On the other hand, average refractive index of the medium with the
579   irregularities increases with respect to that of basic plasma leading to partial compensation of
580   dispersion. The pulse delay and its width decrease with the increase of the electron density
581   variation within irregularity indicating stronger role of the former phenomenon.

582   The results obtained are valid within the framework of the simplifying assumptions
583   made, which should be recalled.

584   First, the approximation of a collisionless and cold background plasma in a uniform
585   magnetic field on a scale of about 30 km is used, which seems to be valid for the conditions of
586   propagation of GHz-range signals (including bipolar nanosecond EMPs) in F2-layer of mid-
587   latitude ionosphere. Plasma frequencies (5 – 10 MHz) and corresponding background plasma
588   densities chosen for simulations (ρ_e = 3 × 10^5 – 10^6 cm^{-3}) are quite typical for F2-layer near its
589   maximum.

590   Second, the ionospheric irregularities are represented by a system of randomly located,
591   field-aligned, cylindrical plasma depletions with sharp boundaries, having the same diameter
592   (20 m) and the same level of perturbation of the electron density relative to the background
593   value (from 5 to 50 percent). In fact, we are considering irregularities of the smallest diameter
594   (according to (Kelly et al., 1995)), the level of density perturbations in which varies from those
595   measured in the experiment (approximately 10 percent) to unrealistically high values. The
596   length of irregularities (30 km in vertical projection) is chosen to be the maximum possible
597   under the conditions of the ionospheric heating experiment. Such irregularity parameters
598   should correspond to the strongest scattering effects for GHz-range radiation.

599   Third, the propagation of an EMP in the form of a quasi-plane electromagnetic wave at
600   an angle of 18 degrees to the magnetic field direction, which corresponds to vertical
601   ionospheric propagation in mid-latitudes, i.e. around the geographical location of the SURA
602   heater. The aperture at which the EMP shape is reconstructed in the presence of density
603   irregularities is of the order of several kilometers, which is sufficient to collect the
604   overwhelming majority of signals scattered by the irregularities in forward direction. Taking into
605   account the spherical shape of the EMP front propagating from a finite-sized source may yield
606   additional effects, but their discussion is beyond the scope of this paper and will be conducted
607   separately.

608   Forth, when simulating the pulse shape after interaction with the irregularities we
609   calculate the phases of separate rays and frequency harmonics, but without taking their
610   polarization into account.

611   When considering the EMP shape for scattering by irregularities, we excluded frequency
612   harmonics below 100 MHz from the analysis. For these harmonics (specifically, from 10 to 100
613   MHz), scattering by density striations is no longer described by the geometric optics
614   approximation. At the same time, these harmonics might be strongly scattered by irregularities
615   and the plasma is transparent for them, therefore, additional grounds are needed to exclude
616   them from analysis. Here, on the one hand, it is necessary to point out once again their

617   extremely small share in the full spectrum of the pulse: less than 0.2 percent in energy. The
618   second significant reason for excluding these harmonics from consideration is the properties of
619   radio wave propagation in the ionosphere with a realistic (non-uniform in height) profile.
620   Indeed, when propagating from the EMP source in the direction of increasing plasma density in
621   the F-layer, spectral harmonics whose frequency is only a few times higher than the maximum
622   plasma frequency will experience strong refraction. Even without irregularities, low-frequency
623   harmonics will drift away from the main high-frequency rays for any finite angle of the ray
624   direction other than strictly vertical propagation. Each act of scattering by an irregularity should
625   lead to a significant deviation of the ray path from the original direction. Furthermore, such
626   harmonics will also experience more pronounced backscattering on irregularities than high-
627   frequency ones. As a result, in addition to their low spectral weight, these harmonics will be
628   further filtered out due to the properties of electromagnetic waves' propagation in ionosphere.
629   As a result, the exclusion of harmonics in the 10-100 MHz range from the analysis of EMPs has,
630   in our opinion, significant physical grounds.

631   Of course, real density striations in heating experiments are characterized by complex
632   statistics, i.e. they have a spread in length, transverse dimensions, depth, as well as various
633   features of spatial distribution, including clustering. At the same time, from elementary
634   geometric-optical analysis it is obvious that the wider the irregularities and the greater the
635   distance between them, the lesser the scattering effects and their influence on the EMP shape.
636   In this sense, the parameters we selected correspond to the narrowest (~10 m) and deepest
637   density irregularities that can be realized, which lead to the strongest scattering effects. We
638   believe that accounting for the spread of irregularities in transverse dimensions or space
639   positions will only further weaken the influence of irregularities on pulse characteristics, which
640   is already small.

641   In general, field-aligned density depletions from 10% (a realistic estimate) to 50% (an
642   overestimate) from the background value and a diameter of about 10 m do not have a
643   significant effect on the EMP shape, which is distorted to a much greater extent due to
644   frequency dispersion. Of course, this result requires clarification in further studies – both in
645   terms of taking into account the effects of radiation depolarization on irregularities, and in
646   terms of taking into account the finite radius of curvature of EMP wave front. However, at this
647   stage it is clear that in the approximation of a plane wave of small amplitude propagating in a
648   cold collisionless plasma, one should not expect a significant influence of scattering effects on
649   the amplitude-temporal and spectral characteristics of EMP in the frequency band of about 1
650   GHz and above.

651

652   **Acknowledgments**

656 **Data Availability Statement**

657 The simulations data are available at https://doi.org/10.5281/zenodo.16687403 [Kirillin 2025].
658

659 **Conflict of Interest**

660

661 The authors have no conflicts to disclose.

662 **References**

663 Agee, F. J., Baum, C. E., Prather, W. D., Lehr, J. M., O'Loughlin, J. P., Burger, J. W., . . . Hull, J. P. (1998). Ultra-
664 wideband transmitter research. *IEEE Transactions on Plasma Science, 26*(3), 860-873.
665 Aol, S., Buchert, S., & Jurua, E. (2020). Ionospheric irregularities and scintillations: a direct comparison of in situ
666 density observations with ground-based L-band receivers. *Earth, Planets and Space, 72*(1), 164.
667 Arnush, D. (1975). Electromagnetic pulse (EMP) propagation through an absorptive and dispersive medium. *IEEE
668 Transactions on Antennas and Propagation, 23*(5), 623-626.
669 Baum, C. E. (1992). From the electromagnetic pulse to high-power electromagnetics. *Proceedings of the IEEE,
670 80*(6), 789-817. doi:10.1109/5.149443
671 Carrano, C. S., Groves, K. M., Caton, R. G., Rino, C. L., & Straus, P. R. (2011). Multiple phase screen modeling of
672 ionospheric scintillation along radio occultation raypaths. *Radio Science, 46*(06), 1-14.
673 Cartwright, N., & Oughstun, K. (2009). Ultrawideband pulse propagation through a homogeneous, isotropic, lossy
674 plasma. *Radio Science, 44*(04), 1-11.
675 Deshpande, K., Bust, G., Clauer, C., Rino, C., & Carrano, C. (2014). Satellite-beacon Ionospheric-scintillation
676 Global Model of the upper Atmosphere (SIGMA) I: High-latitude sensitivity study of the model
677 parameters. *Journal of Geophysical Research: Space Physics, 119*(5), 4026-4043.
678 Dhillon, R., & Robinson, T. (2005). *Observations of time dependence and aspect sensitivity of regions of enhanced
679 UHF backscatter associated with RF heating.* Paper presented at the Annales Geophysicae.
680 Dvorak, S. L., Ziolkowski, R. W., & Dudley, D. G. (1997). Ultra-wideband electromagnetic pulse propagation in a
681 homogeneous, cold plasma. *Radio Science, 32*(1), 239-250.
682 Erukhimov, L., Metelev, S., & Razumov, D. (1988). Diagnostics of ionospheric inhomogeneities with the aid of
683 artificial radio emission. *Radiophysics and Quantum Electronics, 31*(11), 928-934.
684 Erukhimov, L. M., & Mityakov, N. A. (1989). Modification of the ionosphere as a method of its diagnostics In C. H.
685 Liu (Ed.), *World Ionosphere/Thermosphere Study. WITS handbook* (Vol. 2, pp. 267-284). Washington,
686 D.C. : National Science Foundation.
687 Es'kin, V. A., Korobkov, S. V., Gushchin, M. E., & Kudrin, A. V. (2023). Propagation of an ultrawideband
688 electromagnetic pulse along a plasma-filled coaxial line. *IEEE Transactions on Plasma Science, 51*(2),
689 374-380.
690 Fialer, P. (1974). Field-aligned scattering from a heated region of the ionosphere—Observations at HF and VHF.
691 *Radio Science, 9*(11), 923-940.

Franz, T., Kelley, M., & Gurevich, A. (1999). Radar backscattering from artificial field-aligned irregularities. *Radio Science, 34*(2), 465-475.

Frolov, V., Erukhimov, L., Metelev, S., & Sergeev, E. (1997). Temporal behaviour of artificial small-scale ionospheric irregularities: Review of experimental results. *Journal of atmospheric and solar-terrestrial physics, 59*(18), 2317-2333.

Galiègue, H., Féral, L., & Fabbro, V. (2017). Validity of 2-D electromagnetic approaches to estimate log-amplitude and phase variances due to 3-D ionospheric irregularities. *Journal of Geophysical Research: Space Physics, 122*(1), 1410-1427.

Golubev, A. I., Sysoeva, T. G., Terekhin, V. A., Tikhonchuk, V. T., & Altgilber, L. (2000). Kinetic model of the propagation of intense subnanosecond electromagnetic pulse through the lower atmosphere. *IEEE Transactions on Plasma Science, 28*(1), 303-311.

Goykhman, M., Gromov, A., Gundorin, V., Gushchin, M., Zudin, I. Y., Kornishin, S. Y., . . . Loskutov, K. (2022). *Concept and practical implementation of a gigantic plasma-filled coaxial line for simulation of the interaction of electromagnetic pulses with a partially ionized gas medium.* Paper presented at the Doklady Physics.

Grach, S. M., Sergeev, E. N., Mishin, E. V., & Shindin, A. V. (2016) Dynamic properties of ionospheric plasma turbulence driven by high-pow er high-frequency radiowaves. *Phys. Usp., 59*(11), 1091-1128. doi:10.3367/UFNe.2016.07.037868

Hong, J., Chung, J. K., Kim, Y. H., Park, J., Kwon, H. J., Kim, J. H., . . . Kwak, Y. S. (2020). Characteristics of ionospheric irregularities using GNSS scintillation indices measured at Jang Bogo Station, Antarctica (74.62 S, 164.22 E). *Space Weather, 18*(10), e2020SW002536.

Hunsucker, R. D., & Hargreaves, J. K. (2007). *The high-latitude ionosphere and its effects on radio propagation*: Cambridge University Press.

Kelley, M., Arce, T., Salowey, J., Sulzer, M., Armstrong, W., Carter, M., & Duncan, L. (1995). Density depletions at the 10-m scale induced by the Arecibo heater. *Journal of Geophysical Research: Space Physics, 100*(A9), 17367-17376.

Kim, D., Yoon, M., Lee, J., Pullen, S., & Weed, D. (2017). *Monte Carlo simulation for impact of anomalous ionospheric gradient on GAST-D GBAS.* Paper presented at the Proceedings of the ION 2017 Pacific PNT Meeting.

Kirillin, M. Y., Farhat, G., Sergeeva, E. A., Kolios, M. C., & Vitkin, A. (2014). Speckle statistics in OCT images: Monte Carlo simulations and experimental studies. *Optics letters, 39*(12), 3472-3475.

Kirillin, M. (2025). Monte Carlo simulations of nanosecond electromagnetic pulse interaction with field-aligned ionospheric plasma density irregularities: simulation results [Dataset]. Zenodo. https://doi.org/10.5281/zenodo.16687403

Knepp, D. L. (2005). Multiple phase-screen calculation of the temporal behavior of stochastic waves. *Proceedings of the IEEE, 71*(6), 722-737.

Leathers, R. A., Downes, T. V., Davis, C. O., & Mobley, C. D. (2004). Monte Carlo radiative transfer simulations for ocean optics: a practical guide. *Memorandum report A, 426624*(1).

Luchinin, A., & Kirillin, M. Y. (2017). Structure of a modulated narrow light beam in seawater: Monte Carlo simulation. *Izvestiya, Atmospheric and Oceanic Physics, 53*(2), 242-249.

Luchinin, A. G., Dolin, L. S., & Kirillin, M. Y. (2019). Time delay and width variation caused by temporal dispersion of a complex modulated signal in underwater lidar. *Applied Optics, 58*(18), 5074-5081.

Luchinin, A. G., & Kirillin, M. Y. (2021). Angular distribution of photon density waves radiance in media with different scattering anisotropy. *Applied Optics, 60*(31), 9858-9865.

Luchinin, A. G., Kirillin, M. Y., & Dolin, L. S. (2024). Evolution of temporal and frequency characteristics of spherical photon density waves in scattering media. *Journal of Quantitative Spectroscopy and Radiative Transfer, 312*, 108799.

Mahmoudian, A., Scales, W., Taylor, S., Morton, Y., Bernhardt, P., Briczinski, S., & Ghader, S. (2018). Artificial ionospheric gps phase scintillation excited during high-power radiowave modulation of the ionosphere. *Radio Science, 53*(6), 775-789.

Marchuk, G. I., Mikhailov, G. A., Nazareliev, M., Darbinjan, R. A., Kargin, B. A., & Elepov, B. S. (2013). *The Monte Carlo methods in atmospheric optics* (Vol. 12): Springer.

Milikh, G., Gurevich, A., Zybin, K., & Secan, J. (2008). Perturbations of GPS signals by the ionospheric irregularities generated due to HF-heating at triple of electron gyrofrequency. *Geophysical Research Letters, 35*(22).

747 Mountcastle, P. D., & Martin, M. D. (2002). Monte Carlo simulation of ionospheric scintillation. *Proceedings of the*
748   *2002 IEEE Radar Conference* (IEEE Cat. No. 02CH37322), 350 – 355.
749 Mrak, S., Coster, A. J., Groves, K., & Nikoukar, R. (2023). Ground-based infrastructure for monitoring and
750   characterizing intermediate-scale ionospheric irregularities at mid-latitudes. *Frontiers in Astronomy and*
751   *Space Sciences, 10*, 1091340.
752 Najmi, A., Milikh, G., Secan, J., Chiang, K., Psiaki, M., Bernhardt, P., . . . Papadopoulos, K. (2014). Generation and
753   detection of super small striations by F region HF heating. *Journal of Geophysical Research: Space*
754   *Physics, 119*(7), 6000-6011.
755 Nekoogar, F. (2011). *Ultra-Wideband Communications: Fundamentals and Applications Fundamentals and*
756   *Applications*: Prentice Hall Press.
757 Perkins, F. (1975). Ionospheric irregularities. *Reviews of Geophysics, 13*(3), 884-884.
758 Robinson, T. (2002). Effects of multiple scatter on the propagation and absorption of electromagnetic waves in a
759   field-aligned-striated cold magneto-plasma: implications for ionospheric modification experiments.
760   *Annales Geophysicae*, 20, 41-55.
761 Sato, H., Rietveld, M. T., & Jakowski, N. (2021). GLONASS observation of artificial field-aligned plasma
762   irregularities near magnetic zenith during EISCAT HF experiment. *Geophysical Research Letters, 48*(4),
763   e2020GL091673.
764 Schlegel, K. (1973). Monte Carlo simulation of a model ionosphere—II. Energy flow and energy dissipation.
765   *Journal of Atmospheric and Terrestrial Physics, 35*(3), 415-424.
766 Sergeeva, E. A., Kirillin, M. Y., & Priezzhev, A. V. e. (2006). Propagation of a femtosecond pulse in a scattering
767   medium: theoretical analysis and numerical simulation. *Quantum Electronics, 36*(11), 1023.
768 Soldatov, A., & Terekhin, V. (2016). Propagation of an ultrawideband electromagnetic signal in ionospheric plasma.
769   *Plasma Physics Reports, 42*(10), 970-977.
770 Streltsov, A., Berthelier, J.-J., Chernyshov, A., Frolov, V., Honary, F., Kosch, M., . . . Rietveld, M. (2018). Past,
771   present and future of active radio frequency experiments in space. *Space Science Reviews, 214*(8), 118.
772 Wernik, A., Secan, J., & Fremouw, E. (2003). Ionospheric irregularities and scintillation. *Advances in Space*
773   *Research, 31*(4), 971-981.
774 Xiong, G., Xue, P., Wu, J., Miao, Q., Wang, R., & Ji, L. (2005). Particle-fixed Monte Carlo model for optical
775   coherence tomography. *Optics express, 13*(6), 2182-2195.
776 Yan, S., & Fang, Q. (2020). Hybrid mesh and voxel based Monte Carlo algorithm for accurate and efficient photon
777   transport modeling in complex bio-tissues. *Biomedical Optics Express, 11*(11), 6262-6270.
778 Zhang, T., Li, Z., Duan, C., Wang, L., Wei, Y., Li, K., . . . Cao, B. (2024). Design of a High-Power Nanosecond
779   Electromagnetic Pulse Radiation System for Verifying Spaceborne Detectors. *Sensors (Basel, Switzerland),*
780   *24*(19), 6406.
781 Zudin, I., Gushchin, M., Korobkov, S., Strikovskiy, A., Katkov, A., Kochedykov, V., & Petrova, I. (2024).
782   Transformation of the Shape and Spectrum of an Ultrawideband Electromagnetic Pulse in a "Gigantic"
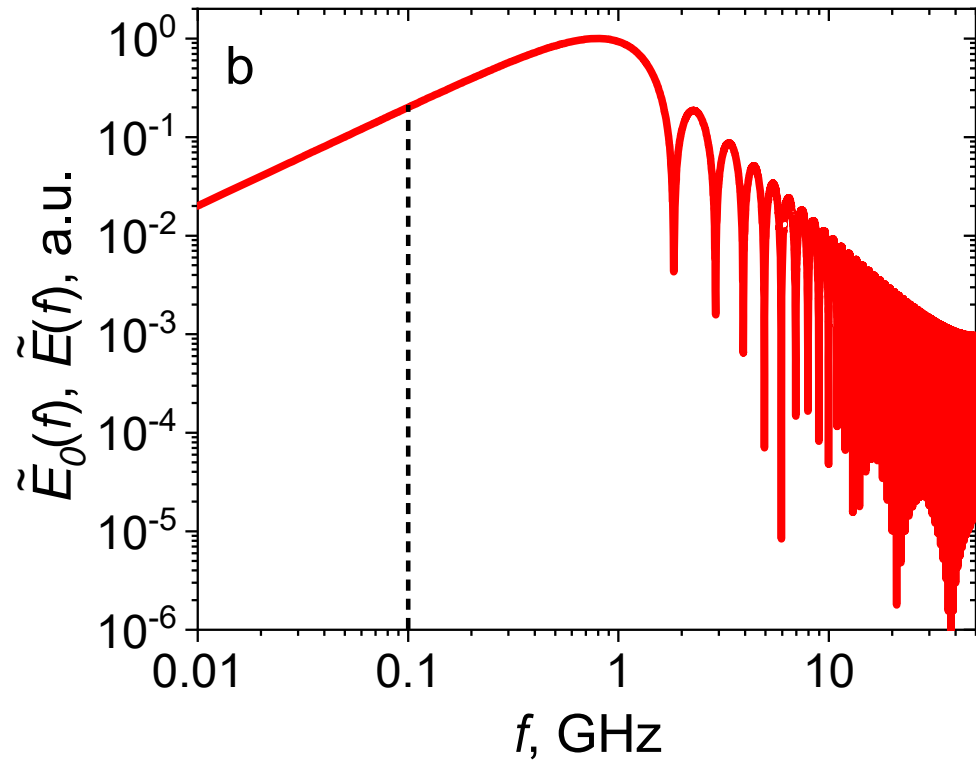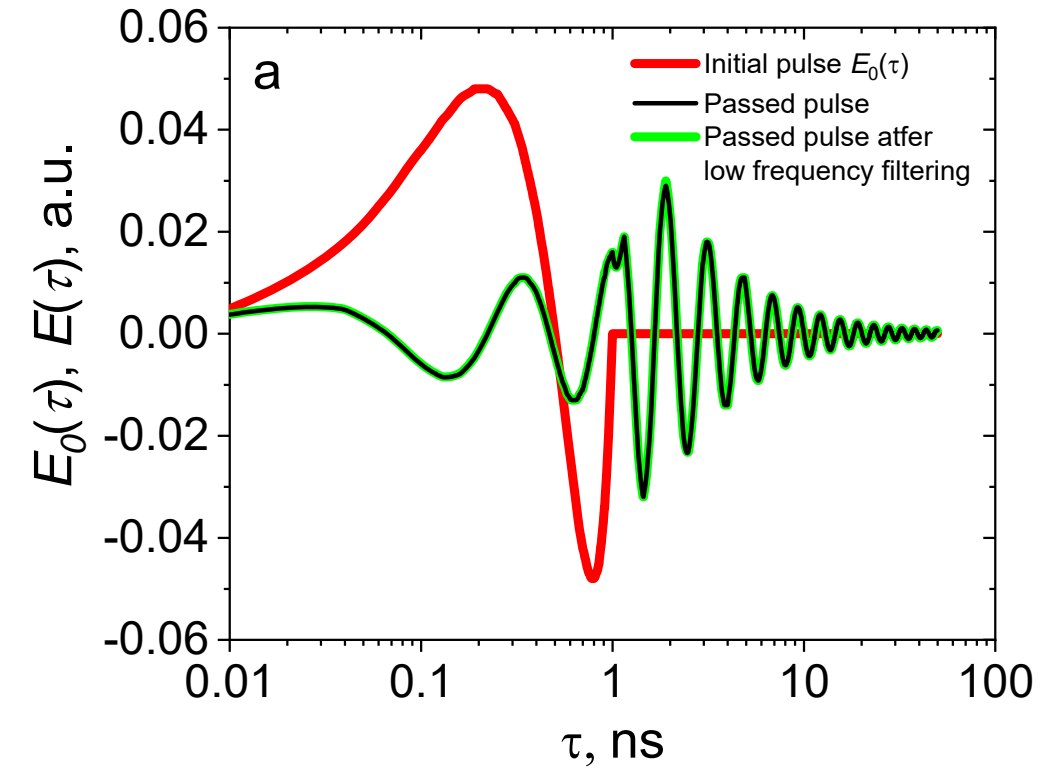783   Coaxial Line Filled with Magnetized Plasma. *Applied Sciences, 14*(2), 705.
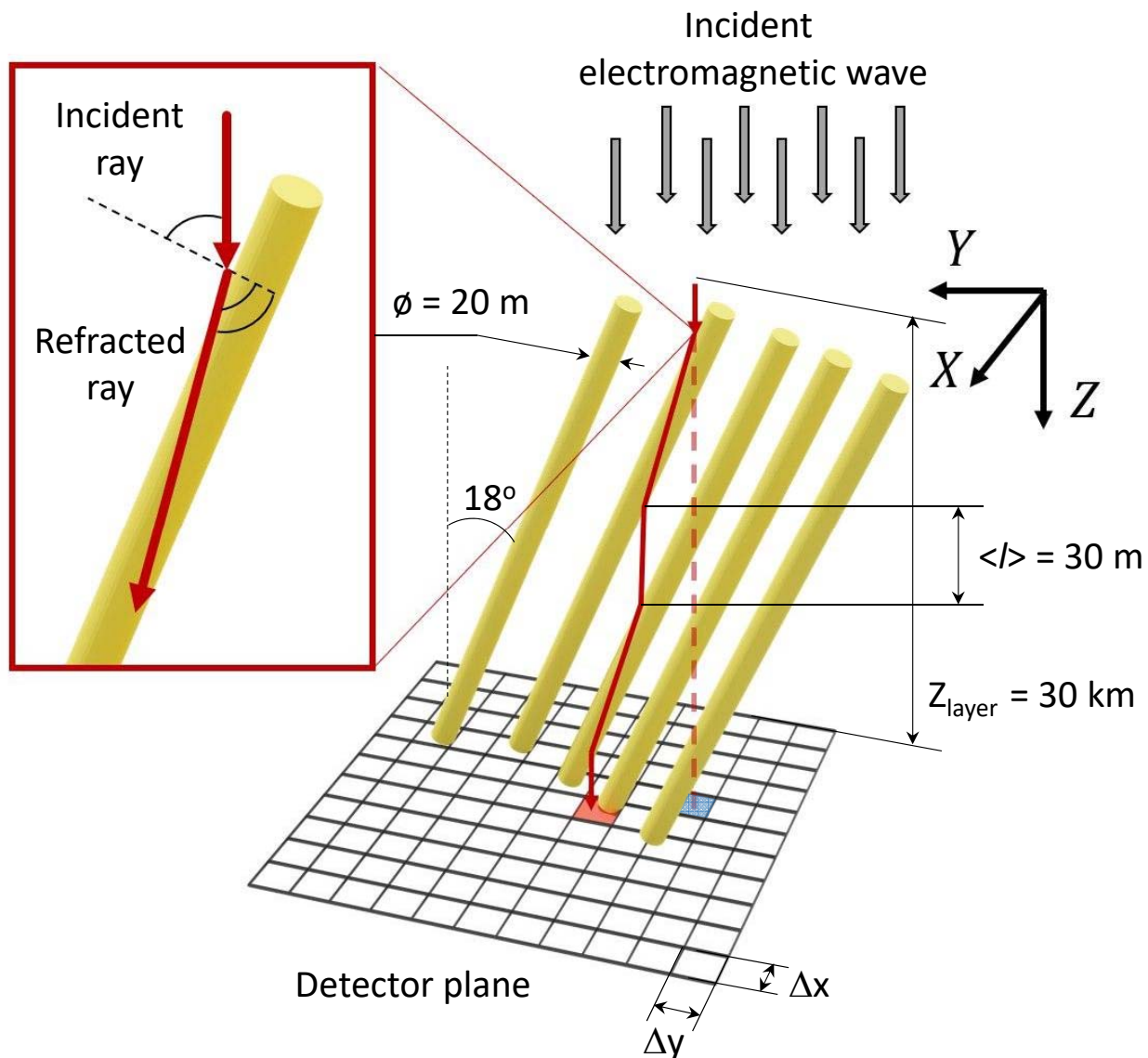784
785

Figure 1.

Figure 2.

Incident
electromagnetic wave

Incident
ray

Refracted
ray

$\emptyset$ = 20 m

18°

Y

X

Z

$<l>$ = 30 m

Z_{layer} = 30 km

Detector plane

Δx

Δy
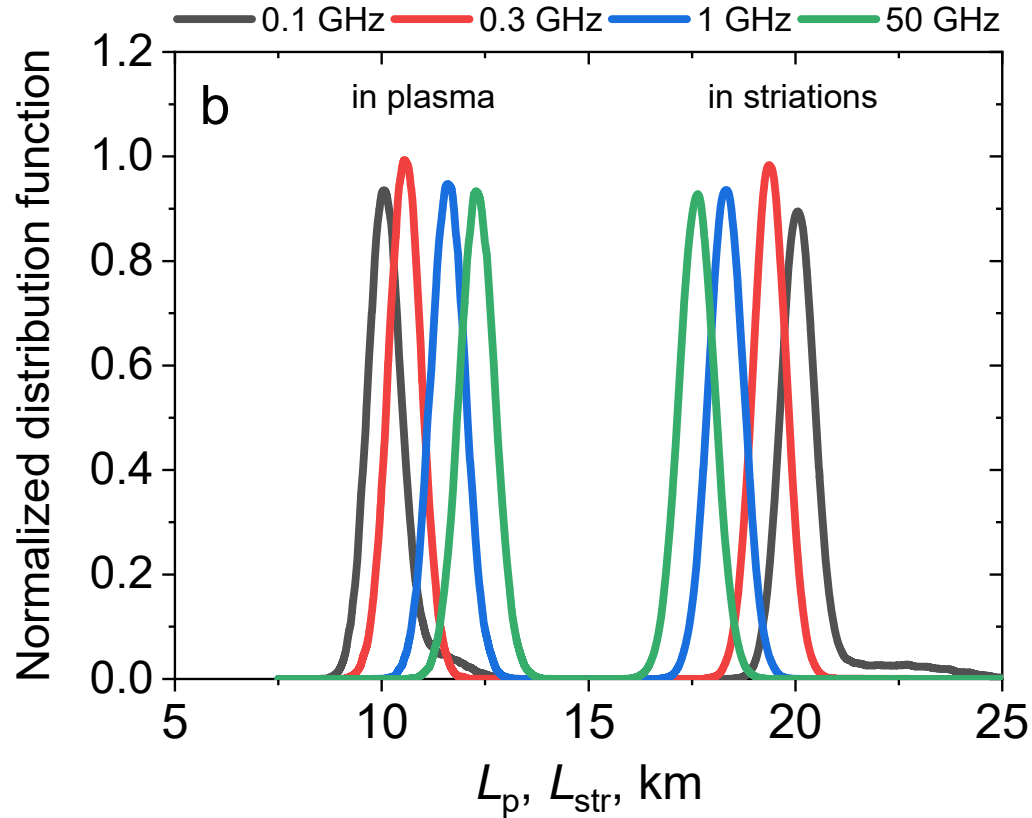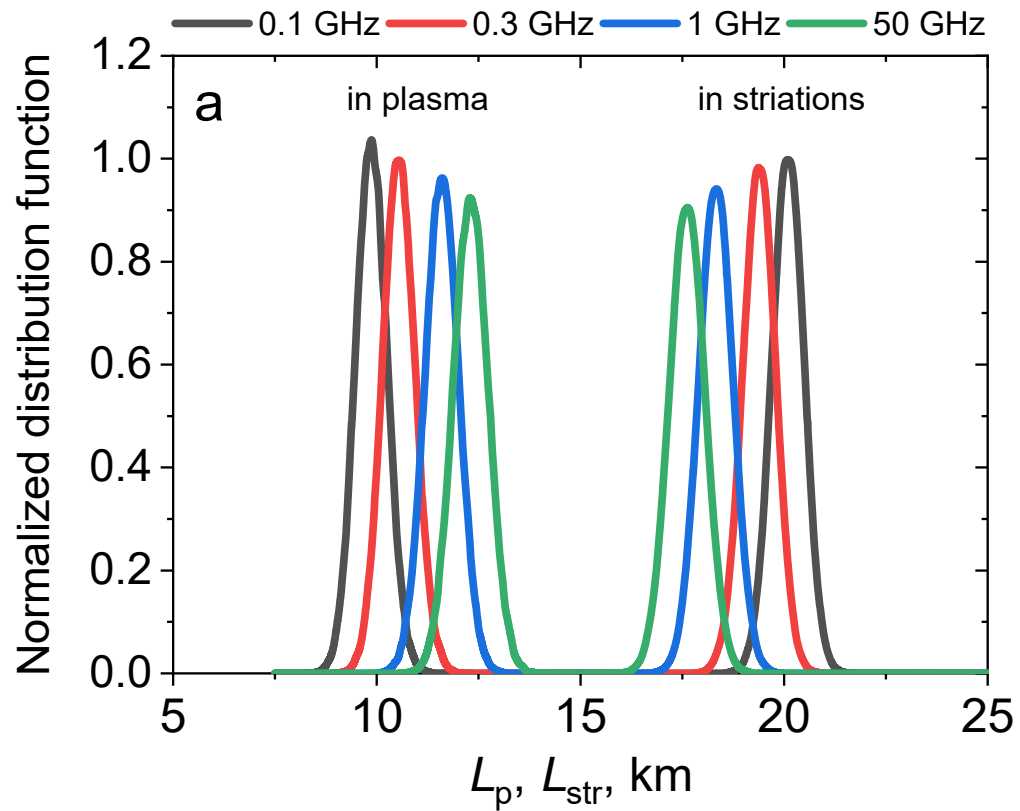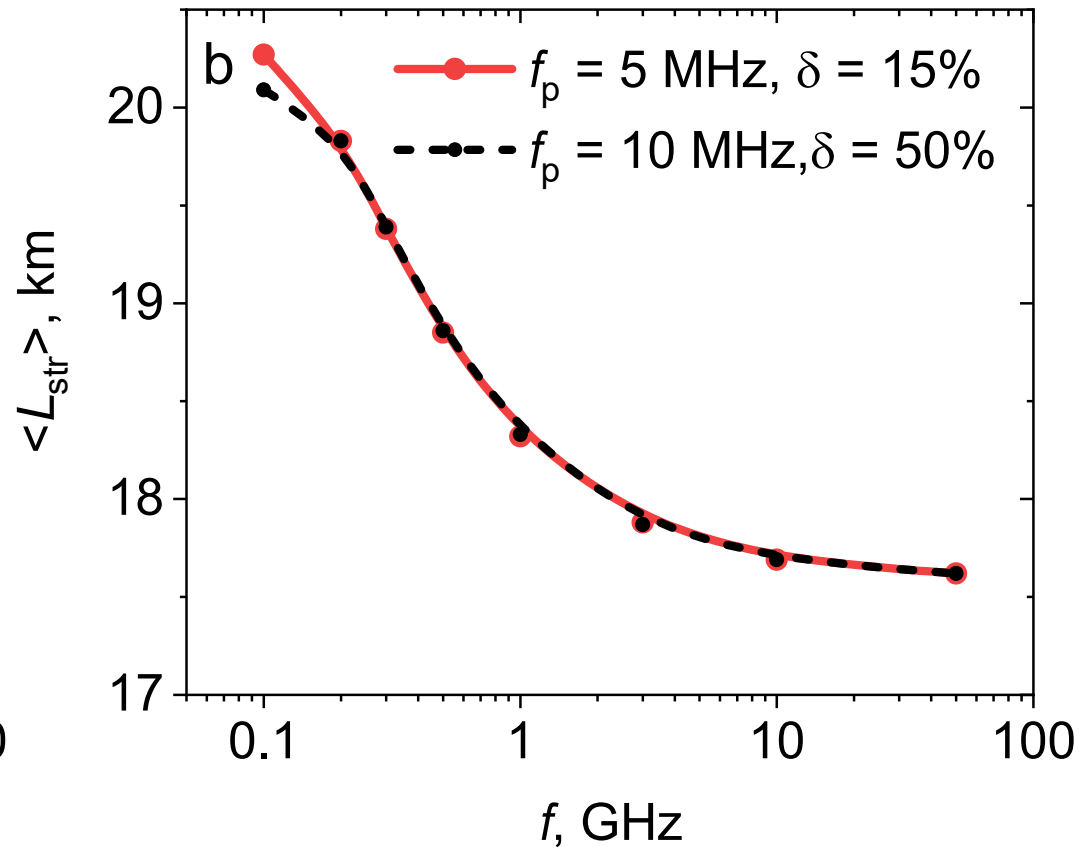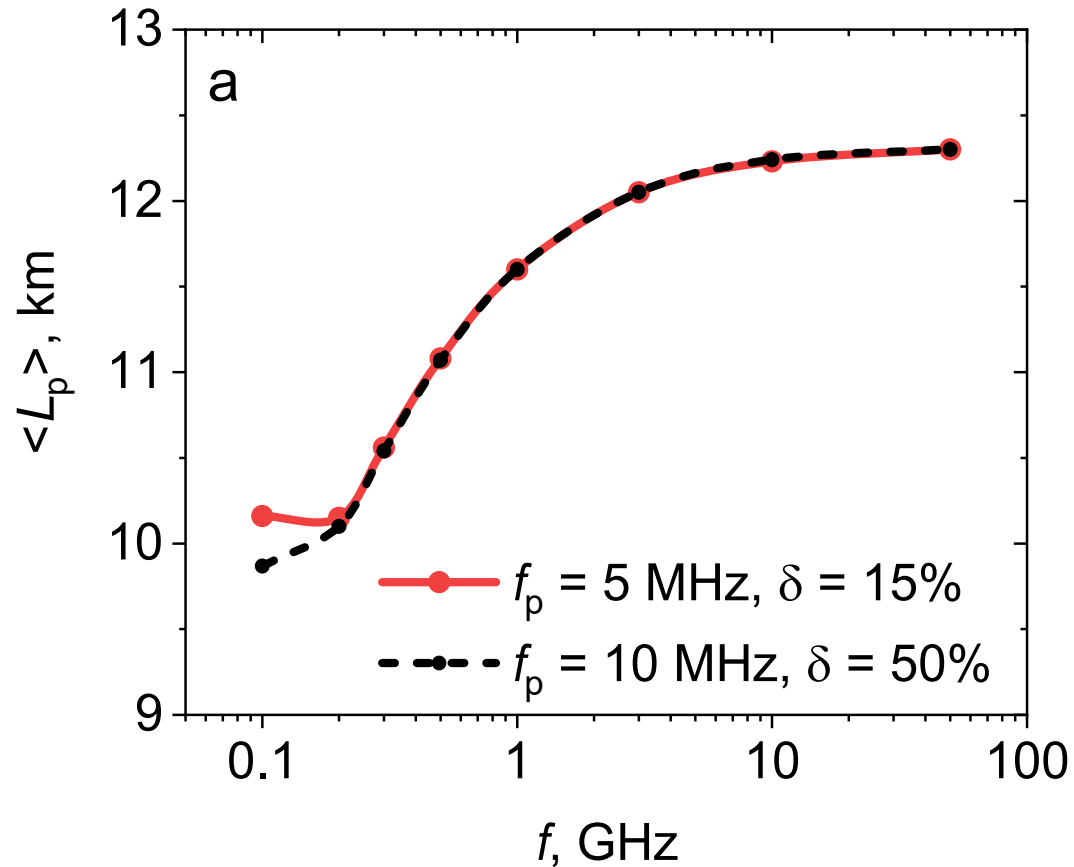
Figure 3.

Figure 4.

Figure 5.
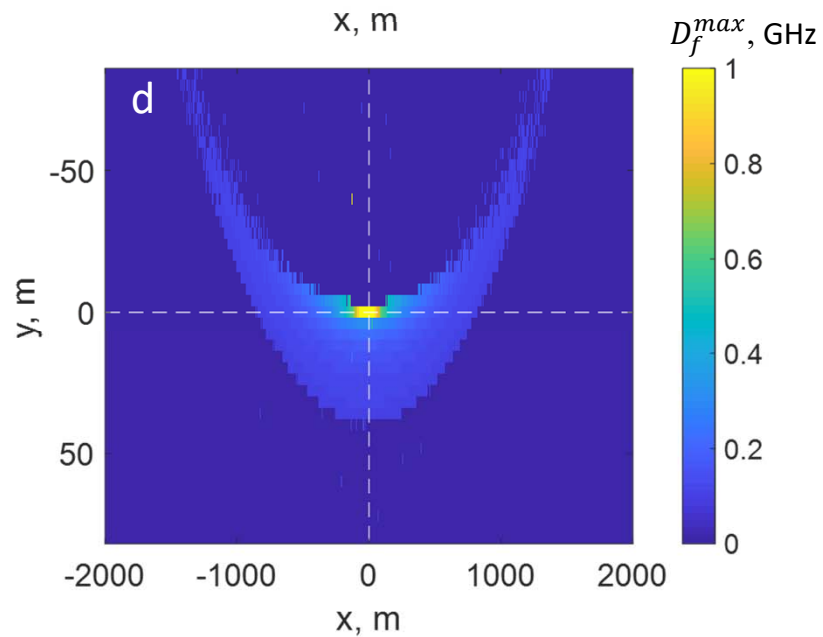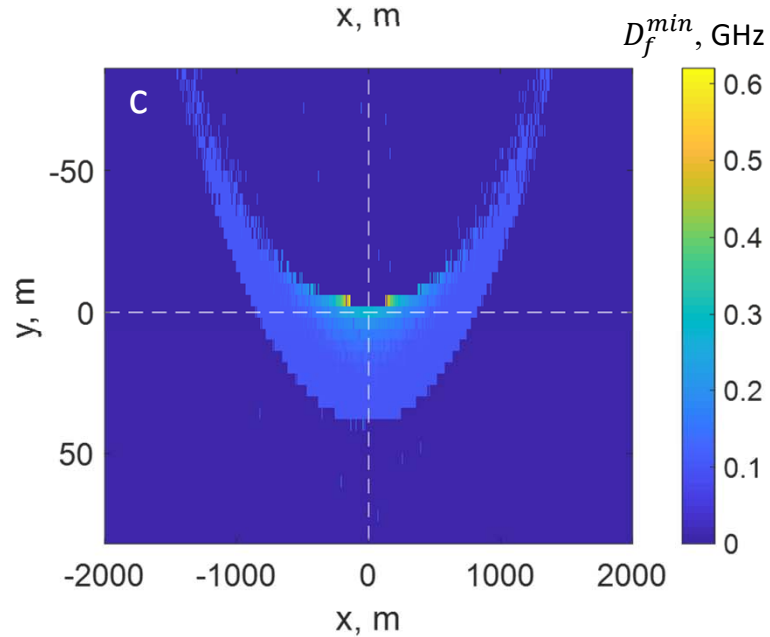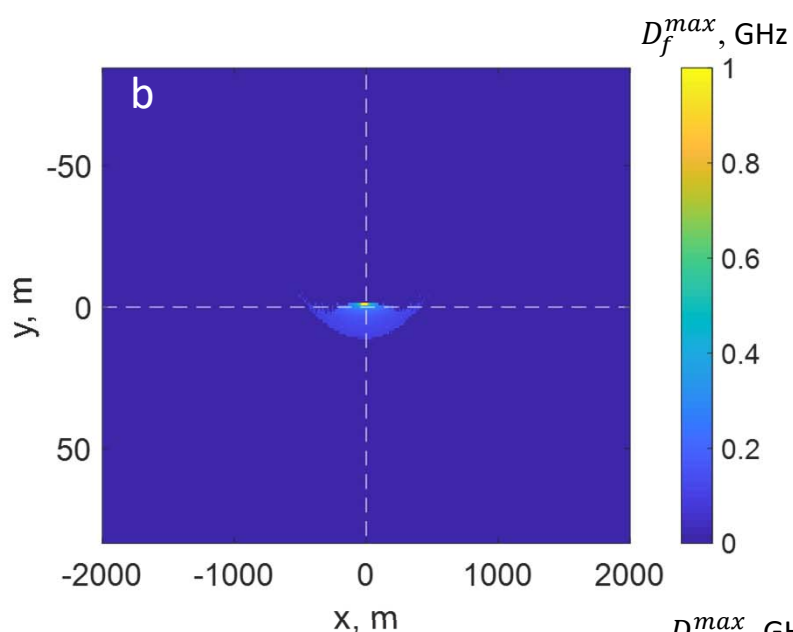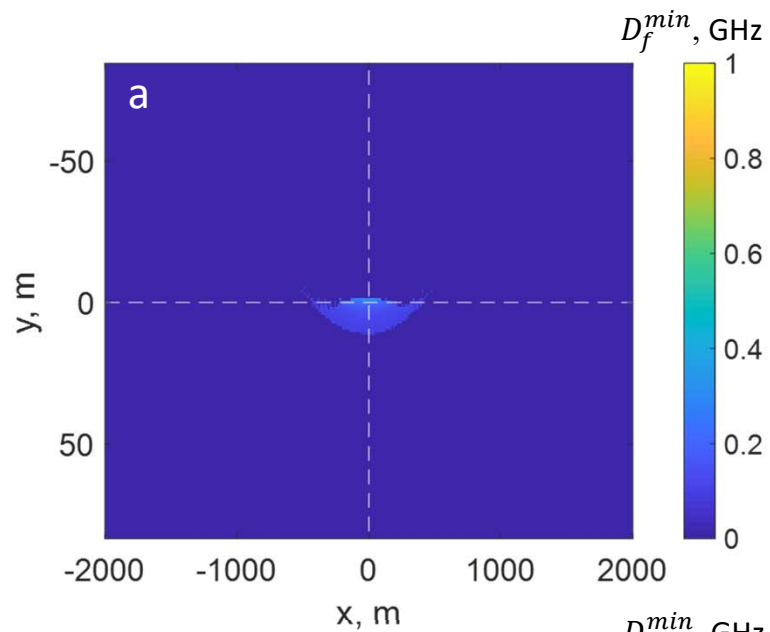
Figure 6.
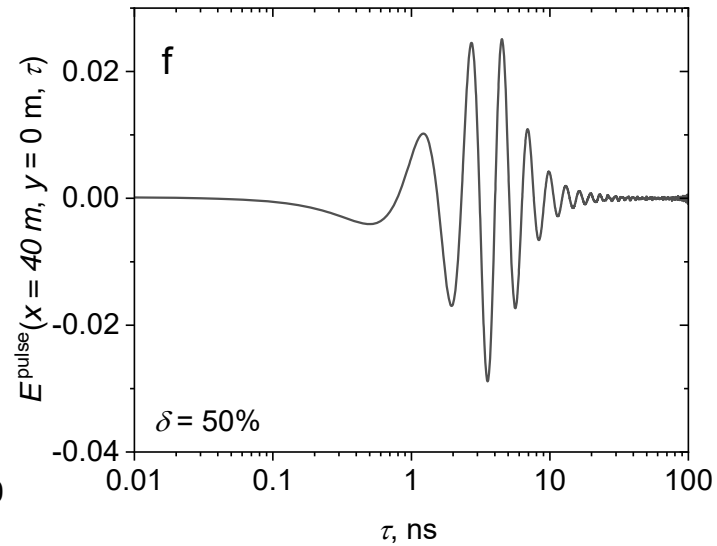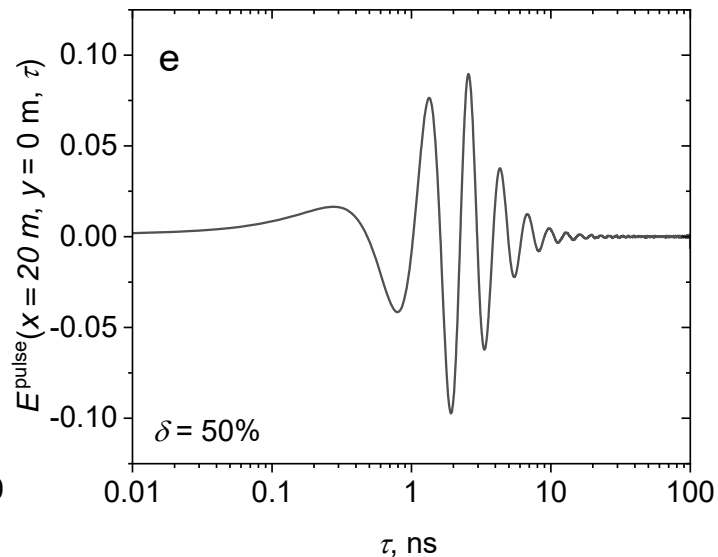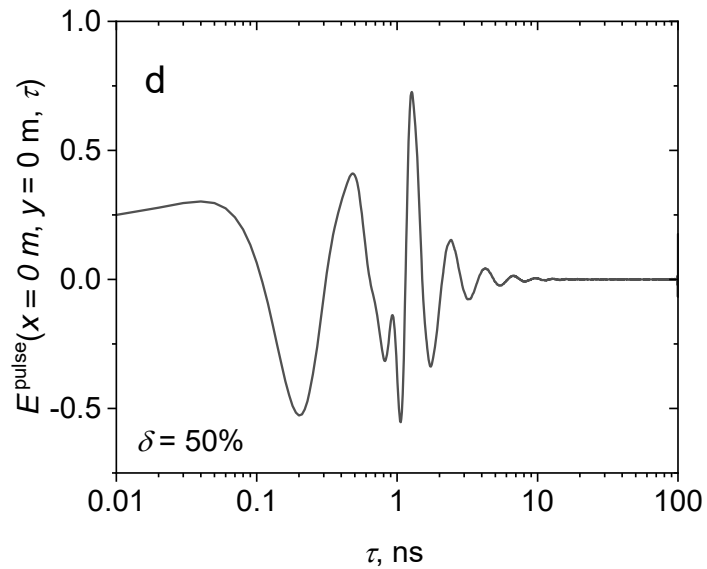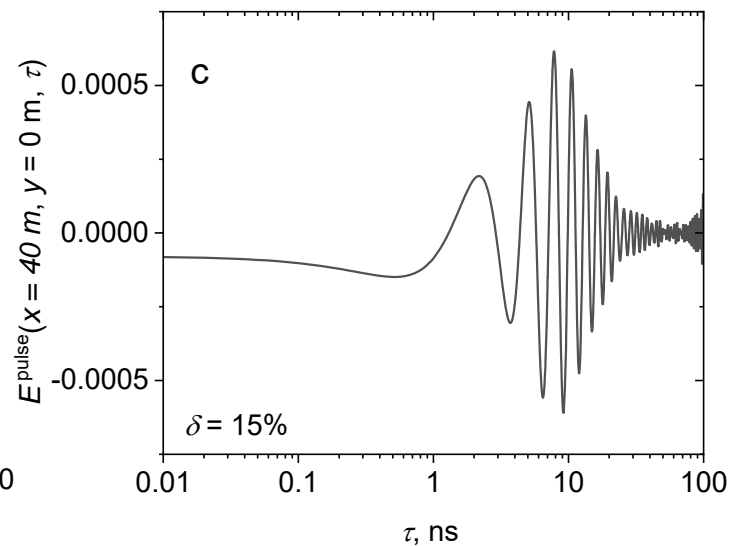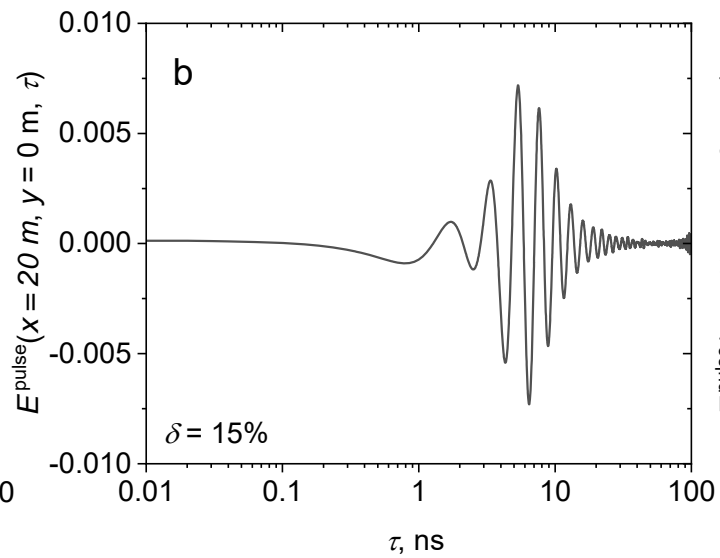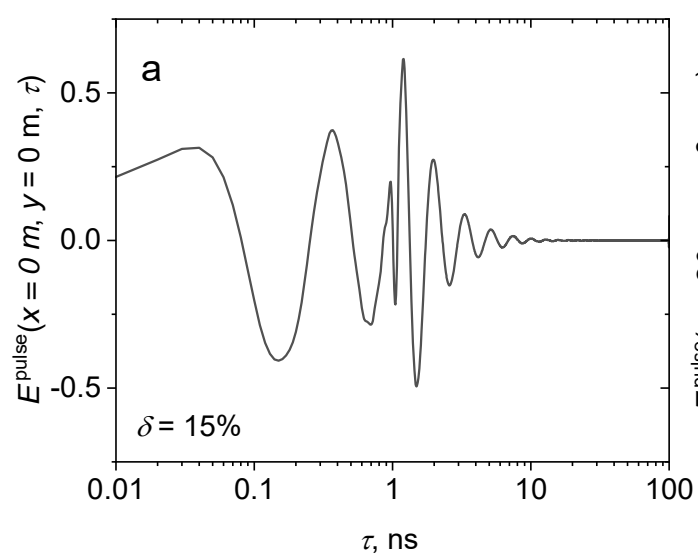
Figure 7.
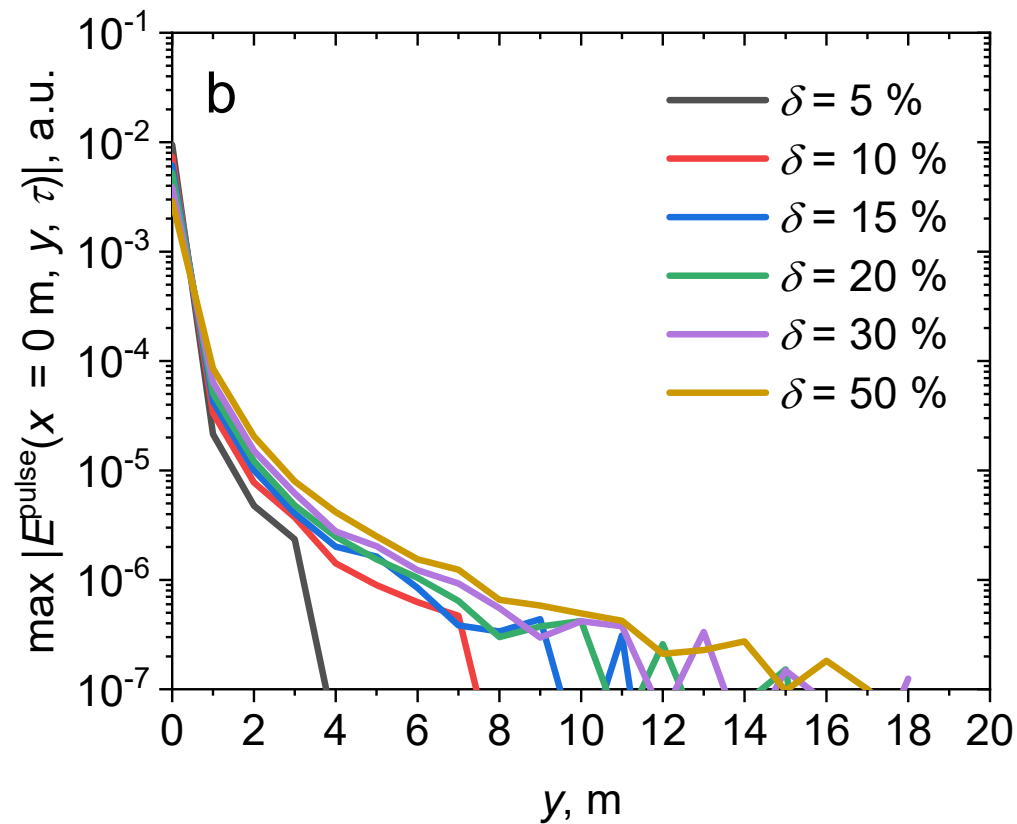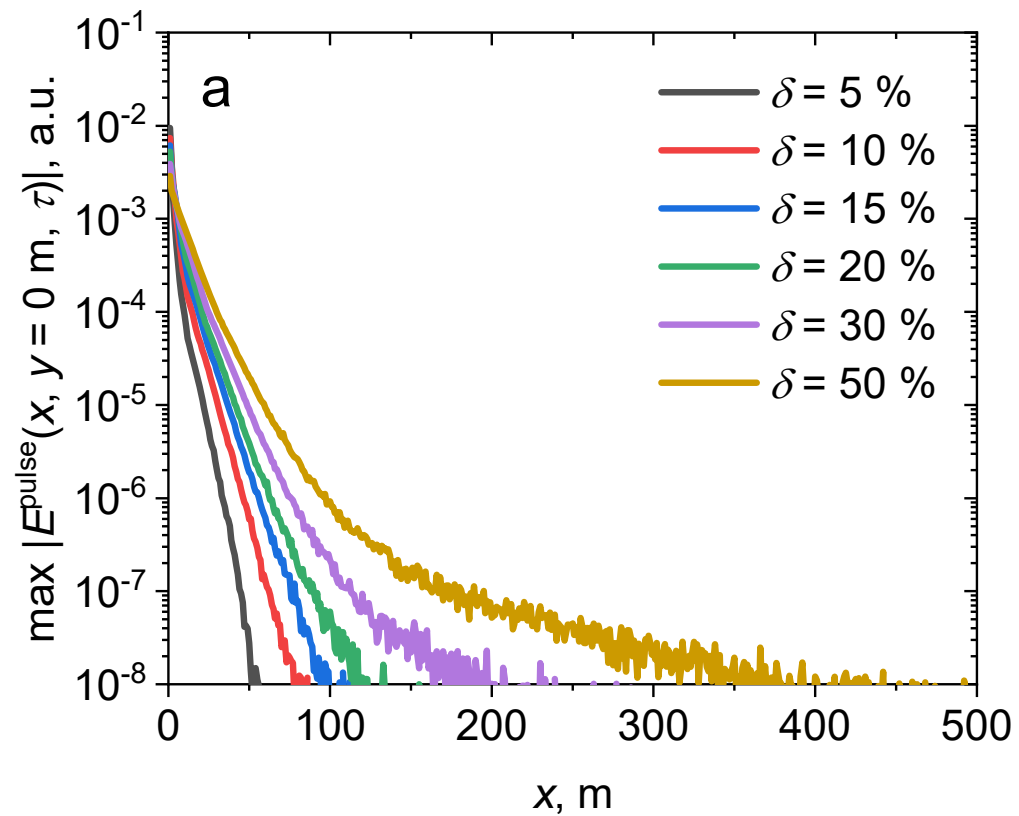
Figure 8.

Figure 9.

Figure 10.

Figure showing panels (a) and (b).

Panel a — Legend:
- f_p = 5 MHz, no scattering (black filled squares)
- f_p = 5 MHz, scattering (red filled squares)
- f_p = 10 MHz, no scattering (black open circles)
- f_p = 10 MHz, scattering (red open circles)

Axes: $\langle\tau\rangle$, ns (vertical); δ, % (horizontal)

Panel b — Legend:
- f_p = 5 MHz, no scattering (black filled squares)
- f_p = 5 MHz, scattering (red filled squares)
- f_p = 10 MHz, no scattering (black open circles)
- f_p = 10 MHz, scattering (red open circles)

Axes: $\Delta\tau$, ns (vertical); δ, % (horizontal)